Department of Applied Physics

Electromagnetic Nanophotonics: Superlens Imaging of Dipolar Emitters and Cloaking in Weak Scattering

Timo Hakkarainen

Aalto University

DOCTORAL DISSERTATIONS

Aalto University publication series
DOCTORAL DISSERTATIONS 151/2012

Electromagnetic Nanophotonics: Superlens Imaging of Dipolar Emitters and Cloaking in Weak Scattering

Timo Hakkarainen

A doctoral dissertation completed for the degree of Doctor of Science in Technology to be defended, with the permission of the Aalto University School of Science, at a public examination held in Auditorium F239a of the F building (Otakaari 3, Espoo, Finland) on the 30th of November 2012 at 12 noon.

Aalto University
School of Science
Department of Applied Physics
Optics and Photonics

Supervising professor
Professor Ari T. Friberg

Thesis advisor
Docent Tero Setälä

Preliminary examiners
Professor Martti Kauranen
Tampere University of Technology, Finland
Professor Karl-Heinz Brenner
University of Heidelberg, Germany

Opponent
Professor Micheal A. Fiddy
University of North Carolina, USA

Aalto University publication series
DOCTORAL DISSERTATIONS 151/2012

ISBN 978-952-60-4868-0 (printed)
ISBN 978-952-60-4869-7 (pdf)
ISSN-L 1799-4934
ISSN 1799-4934 (printed)
ISSN 1799-4942 (pdf)
http://urn.fi/URN:ISBN:978-952-60-4869-7

Unigrafia Oy
Helsinki 2012

Finland

Publication orders (printed book):
timo.hakkarainen@aalto.fi

Aalto University

Abstract

Aalto University, P.O. Box 11000, FI-00076 Aalto www.aalto.fi

Author
Timo Hakkarainen

Name of the doctoral dissertation
Electromagnetic Nanophotonics: Superlens Imaging of Dipolar Emitters and Cloaking in Weak Scattering

Publisher School of Science

Unit Department of Applied Physics

Series Aalto University publication series DOCTORAL DISSERTATIONS 151/2012

Field of research Engineering Physics, Physics

Manuscript submitted 21 August 2012 **Date of the defence** 30 November 2012

Permission to publish granted (date) 29 October 2012 **Language** English

☐ **Monograph** ☒ **Article dissertation (summary + original articles)**

Abstract

Two novel topics of nanophotonics, near-field imaging by superlenses and invisibility cloaking with slab scatterers, are investigated within the context of classical electromagnetic theory.

In superlens imaging the objects are radiating point dipoles or externally excited dipolar emitters. The imaging element is a metallic or a slightly lossy negative-index material (NIM) slab with thickness of a few tens of nanometers. The electromagnetic angular spectrum representation is used to derive the Green tensors for the slab's transmission and reflection. With this formalism the point-spread function of the imaging system is numerically evaluated, which enables one to assess resolution and image brightness. The dependence of image quality on the system parameters, dipole orientations, and near-field interactions among the objects and the lens is investigated.

It is shown that both metallic and lossy metamaterial superlenses allow for image definitions beyond the usual diffraction limit of half the wavelength λ. High image quality requires a low-absorption slab and a good impedance match of the lens and its surroundings. In the immediate vicinity of the slab the dipole-slab interaction prevents the dipole from radiating. With low-loss NIM the interaction is weak and of short range. For silver slabs the interaction is stronger and reaches over the near-field zone, adversely influencing the imaging capabilities. With two dipole-like objects the emission is also suppressed by dipole-dipole near-field interactions, in particular with molecular objects while the effect is weak for glass or metallic nanoparticles. Due to interference subwavelength definition can only be attained for dipoles aligned predominantly orthogonal to the slab. Such a situation is achieved with excitation by total internal reflection. In optimal circumstances, resolutions of about $\lambda/5$ for silver and $\lambda/10$ for metamaterial lens are reached in three-dimensional configurations.

Invisibility cloaking is considered within weak optical scattering in slab geometry. The conditions for cloaking in forward and backward directions are established, enabling the determination of the cloak's refractive-index distribution for stratified objects. For any absorbing object forward cloaking is achieved with a lossy NIM or gainy ordinary-material slab. The cloaking is perfect for incident fields of any spatial structure and bandwidth. Backward cloaking is found possible with self-imaging fields. In both cases the cloak's dispersive properties resemble those of the object.

Keywords near-field optics, superlens imaging, optical scattering

ISBN (printed) 978-952-60-4868-0 **ISBN (pdf)** 978-952-60-4869-7

ISSN-L 1799-4934 **ISSN (printed)** 1799-4934 **ISSN (pdf)** 1799-4942

Location of publisher Espoo **Location of printing** Helsinki **Year** 2012

Pages 140 **urn** http://urn.fi/URN:ISBN:978-952-60-4869-7

A? Aalto-yliopisto

Tiivistelmä

Aalto-yliopisto, PL 11000, 00076 Aalto www.aalto.fi

Tekijä
Timo Hakkarainen

Väitöskirjan nimi
Sähkömagneettinen nanofotoniikka: dipolilähteiden kuvaaminen superlinsseillä ja heikosti sirottavien kohteiden häivyttäminen

Julkaisija Perustieteiden korkeakoulu

Yksikkö Teknillisen fysiikan laitos

Sarja Aalto University publication series DOCTORAL DISSERTATIONS 151/2012

Tutkimusala Teknillinen fysiikka, fysiikka

Käsikirjoituksen pvm 21.08.2012 **Väitöspäivä** 30.11.2012

Julkaisuluvan myöntämispäivä 29.10.2012 **Kieli** Englanti

☐ **Monografia** ☒ **Yhdistelmäväitöskirja (yhteenveto-osa + erillisartikkelit)**

Tiivistelmä

Työssä tutkitaan klassista sähkömagneettista teoriaa käyttäen kahta modernin nanofotoniikan aihetta: lähikenttäkuvaamista superlinsseillä ja kohteen häivyttämistä.

Superlinsseillä kuvattaessa objektina toimii säteilevä pistedipoli tai dipolimainen sirottaja. Kuvauslinssinä käytetään metallista tai häviöllisestä metamateriaalista koostuvaa levyä, jonka paksuus on kymmenien nanometrien suuruusluokkaa. Työssä johdetaan Greenin tensorit levyn läpäisylle ja heijastukselle sähkömagneettisen kulmaspektriesityksen avulla. Tällä formalismilla lasketaan numeerisesti dipolin kuvajakauma, mikä mahdollistaa kuvan kirkkauden ja tarkkuuden määrittämisen. Tarkasteltavana on syntyneen kuvan laadun riippuvuus kuvaussysteemin parametreista, objektidipolien suunnasta sekä objektien ja linssin välisistä lähikenttävuorovaikutuksista.

Työssä osoitetaan, että puolen aallonpituuden (λ) kuvaustarkkuus voidaan ylittää metalli- ja metamateriaalisuperlinsseillä. Terävä kuva edellyttää pienihäviöistä kuvauselementtiä sekä hyvää impedanssien sovitusta elementin ja ympäristön välillä. Linssin välittömässä läheisyydessä objekti-linssi -vuorovaikutukset heikentävät dipolilähteen säteilyn voimakkuutta. Metamateriaalilinssille ilmiö on heikko, mutta metallilinssin tapauksessa se on merkittävä ja kattaa lähikenttäalueen heikentäen elementin kuvausominaisuuksia. Myös kahden molekyylimäisen objektin vuorovaikutukset vähentävät emissiota, kun taas lasi- ja metallinanohiukkasia kuvattaessa näin ei käy. Interferenssin johdosta alle puolen aallonpituuden kuvaustarkkuus saavutetaan vain, jos dipolit osoittavat kohtisuoraan kuvauslevyä kohti. Tämä saadaan aikaan virittämällä dipolit kokonaisheijastuksella luodulla vaimenevalla kentällä. Optimaalisessa tilanteessa kolmidimensioisella kuvaussysteemillä päästään kuvaustarkkuuteen, joka on noin $\lambda/5$ metallilinssille ja $\lambda/10$ metamateriaalilinssille.

Työssä tarkastellaan heikosti valoa sirottavien objektien häivyttämistä levygeometriassa. Ilmiölle määritetään tarkastelusuunnasta riippuvat ehdot, jotka mahdollistavat häivemateriaalin taitekertoimen laskemisen. Kerrosrakenteinen objekti voidaan saattaa edestäpäin näkymättömäksi häviöllisellä metamateriaalilla tai vahvistavalla aineella. Häivyttäminen on täydellistä ja toteutuu mielivaltaiselle valaistukselle. Myös heijastuksessa objektin näkymättömäksi tekeminen on mahdollista, mutta vain itsekuvautuvien kenttien tapauksessa. Häivemateriaalin dispersiiviset ominaisuudet määräytyvät objektin vastaavista ominaisuuksista.

Avainsanat lähikenttäoptiikka, superlinssikuvaus, optinen sironta

ISBN (painettu) 978-952-60-4868-0 **ISBN (pdf)** 978-952-60-4869-7

ISSN-L 1799-4934 **ISSN (painettu)** 1799-4934 **ISSN (pdf)** 1799-4942

Julkaisupaikka Espoo **Painopaikka** Helsinki **Vuosi** 2012

Sivumäärä 140 **urn** http://urn.fi/URN:ISBN:978-952-60-4869-7

Preface

In my first grade of the elementary school I remember feeling frustrated in maths class when we were told to color three apples out of five. I asked the teacher to give me a more difficult problem to solve. I do not remember the formulation of this highly demanding task she gave me but I remember the solution. It was 18.

Eighteen years later, in 2008, I started my PhD studies, now with more questions than solutions. My four-year research is summarized in this dissertation, and it has been carried out in the Department of Applied Physics of Aalto University School of Science. Now, I want to take this opportunity to thank some people for their support during the project.

I am most indebted to my supervisor Professor Ari T. Friberg. Your persistent support and knowledge on electromagnetics has been an indispensable advantage. I have learned from you a great deal about optics, research work in general, and of leadership. Your endless enthusiasm towards research projects and your way to challenge students' thinking inspire the rest of Theory Group. I am also very grateful to my instructor, Docent Tero Setälä, for his guidance along the way and for believing in my ability to complete this thesis. Further, I thank Professor Matti Kaivola for the opportunity to work in the department.

During the course of this work I have had the pleasure to collaborate with many talented people in the Optics and Photonics Group. I wish to thank Dr. Markus Hautakorpi, Dr. Klas Lindfors, and Doc. Andriy Shevchenko for insightful discussions on optics. I am also grateful to M.Sc. Henri Kellock, M.Sc. Kimmo Kokkonen, M.Sc. Lauri Lipiäinen, Dr. Esa Räikkönen, M.Sc. Timo Voipio, and Orvokki Nyberg for many valuable advice in practical matters. Special thanks go to my workmates, M.Sc. Andreas Norrman and Dr. Arri Priimägi, who have had positive influence on my well-being with common interests also beyond optics.

I am also fortunate to have many important friends who, each in their unique way, have supported me during this work. First, I wish to express my gratitude for two of them, M.Sc. Teemu Hakkarainen and M.Sc. Juha Pirkkalainen, who are talented physicists and with whom I have shared invaluable thoughts during our paths in university studies. I also want to thank a bunch of inspiring and sparkling people, Anna, Anssi, Elina, Ilmari, Jani, Jere, Juho, Jukka, Kaisa, Lasse, Lauri K., Mari H., Mari K., Pälvi, and Tero K. You all have enriched my life with performing arts, music, traveling, wandering in nature, thoughtful conversations, and with a couple of obscure dusk-till-dawn adventures.

I wish to acknowledge the Finnish Graduate School of Modern Optics and Photonics and the Academy of Finland for funding my doctoral research. In addition, personal grants from the Finnish Foundation for Technology Promotion and Emil Aaltonen Foundation are gratefully appreciated.

I am deeply grateful to my dear parents and sisters for their constant support and encouragement throughout my life. Most of all, I would like to thank Marjo, my lovely, little creature and companion in life, for her endless patience and love during this work.

Helsinki, October 31, 2012,

Timo Hakkarainen

Contents

List of Publications

This thesis consists of an overview and of the following publications which are referred to in the text by their Roman numerals.

I Timo Hakkarainen, Tero Setälä, and Ari T. Friberg. Subwavelength electromagnetic near-field imaging of point dipole with metamaterial nanoslab. *Journal of the Optical Society of America A* **26**, 10, 2226–2234, September 2009.

II Timo Hakkarainen, Tero Setälä, and Ari T. Friberg. Near-field imaging of point dipole with silver superlens. *Applied Physics B* **101**, 4, 731–734, July 2010.

III Timo Hakkarainen, Tero Setälä, and Ari T. Friberg. Electromagnetic near-field interactions of a dipolar emitter with metal and metamaterial nanoslabs. *Physical Review A* **84**, 3, 033849, September 2011.

IV Timo Hakkarainen, Tero Setälä, and Ari T. Friberg. Near-field imaging of interacting nano objects with metal and metamaterial superlenses. *New Journal of Physics* **14**, 043019, April 2012.

V Tero Setälä, Timo Hakkarainen, Ari T. Friberg, and Bernhard J. Hoenders. Object-dependent cloaking in the first-order Born approximation. *Physical Review A* **82**, 1, 013814, July 2010.

Author's Contribution

The author has had a key role in all aspects of the research work summarized in this thesis and reported in Publications I–V.

Publications I–IV

The author has performed all the analytical calculations, as well as the numerical implementations. The author has had a major role in the interpretation of the results, and he has written the first versions of the manuscripts.

Publication V

The author has strongly contributed to the analytical and numerical calculations. He has participated in the interpretation of the results and in writing the manuscript.

Another publication to which the author has contributed:

A. Hakola, T. Hakkarainen, R. Tommila, and T. Kajava. Energetic Bessel-Gauss pulses from diode-pumped solid-state lasers. *Journal of the Optical Society of America B* **27**, 11, 2342–2349, November 2010.

In addition to the publications in peer-reviewed journals, the author has presented the research summarized in the thesis in several national and international[1] conferences.

1

EOS Annual Meeting, Paris, 2008;
4th EOS Topical Meeting on Advanced Imaging Techniques, Jena, 2009;
3rd Congress on Advanced Electromagnetic Materials in Microwaves and Optics, London, 2009;
META'10, 2nd Conference on Metamaterials, Photonic Crystals and Plasmonics, Cairo, 2010;
4th Congress on Advanced Electromagnetic Materials in Microwaves and Optics, Karlsruhe, 2010;
Biomedical Optics, Miami, 2012

1. Introduction

The current knowledge to tailor material properties has enabled the generation of novel photonic media with artificially engineered nano-scale structures. These materials are known as metamaterials and they exhibit optical properties not found in natural media [1–3]. Especially in the microwave regime but recently also at optical frequencies, metamaterials have brought a diverse amount of engrossing physics and potential applications into the focus of scientists [4–6]. In particular, the possibility of near-field superlenses providing subwavelength image definition would have significant applications in several fields of technology and science, e.g., optical nano-scale microscopy and biosensing, ultra-accurate optical lithography, and data storage [7]. Another interesting topic born with the metamaterials is optical cloaking: an object is made invisible or less detectable to observer by covering it with a proper material [8, 9]. The theoretical work of my thesis arose from the interest of the Optics and Photonics Group at Aalto University School of Science on these two novel and challenging research fields. The work may be seen as a natural extension for the group's long experience to apply classical electromagnetic theory to research problems of nanophotonics.

The resolution in conventional (far-field) optical imaging is limited by the wavelength of light (λ) and the numerical aperture (NA) of the system [10]. However, optical imaging beyond the classic Rayleigh–Abbe diffraction limit of $\lambda/2$ in spatial resolution has long been a subject of interest to scientists [10, 11]. This limit emerges because the information on the finest features of the object is carried by the high-spatial-frequency waves, known as evanescent waves, which decay exponentially. So, not even the best of the far-field lenses can collect the evanescent waves in the image. The advent of near-field optics has brought out various methods that allow one to catch the evanescent modes and the associated subwavelength

information [10–12]. A widely employed approach in nanophotonics is optical near-field microscopy, which makes use of scanning local probes and near-field imaging elements [12]. In these techniques the imaging device is placed at a subwavelength distance from the object, enabling detection of the evanescent field created by the object and thereby increasing the effective NA.

During the past ten years, near-field imaging with metallic and metamaterial superlenses has inspired an increasing number of works [7] following the suggestion of the 'perfect lens' [13]. The perfect lens (in air) is a lossless nanoslab having its relative electric permittivity and magnetic permeability equal to -1. It is an idealized case of negative-index materials (NIMs) that are characterized by negative refractive index. Such a lens cancels the phase changes accumulated by propagating waves and restores the evanescent wave contributions, and thus delivers an undistorted image with unlimited definition. However, any realistic metamaterial is necessarily lossy leading to absorption of the object radiation and to interactions between the lens and the object which degrades image resolution. Lenses that take the practical limitations into account, and yet allow resolution well beyond the wavelength of the light (deep-subwavelength resolution), are known as superlenses. Despite the rapid progress on metamaterials, experimental NIM-lens realizations are few [6, 7]. Besides NIM lenses, subwavelength imaging can be achieved with metallic nanoslabs exhibiting plasmon resonances [7, 13]. The first experimental demonstrations of silver superlenses with subwavelength resolution (about $\lambda/6$) were reported in 2005 [14, 15]. Recently an improved silver-lens design, providing $\lambda/12$ resolution in imaging of a two-dimensional grating object, was fabricated [16].

To make things invisible has always attracted people. The invention of metamaterials has brought this dream from science fiction closer to daily life [8, 9]. In 2006, it was found that an artificial medium having spatially changing optical properties could bend light in extraordinary manners. One example of this is an optical cloak which guides light around an object, similarly to the flow of water around a stone, making the object invisible or less detectable. The possibility to design artificial cloaking materials relies on a variety of mathematical techniques, the best known of which is transformation optics [17, 18]. The breakthrough in cloaking launched what can safely be called a boom among the scientists: the first cloaking device operating at microwave frequencies was realized shortly

after the invention of cloaking [19], and theoretical researches on new geometries pushing the concept towards the optical frequencies have been published at an accelerating rate [8, 9]. The early cloaking schemes suffer from high losses and narrow operation bandwidth, but new designs have enabled low-loss and broad-band optical cloaks [20–22]. Striking proposals of space-time electromagnetic cloaks, concealing not just objects in space but also events in time, have recently been put forward [23, 24].

The major part of this thesis concentrates on near-field imaging with metallic and metamaterial superlenses. We consider dipolar objects creating electric fields with three orthogonal components that are imaged by planar slab lenses in three dimensions. Our main aim is to find out the optimal conditions for the imaging in terms of resolution and brightness. In Publications I–IV we develop a detailed theoretical formalism for this purpose and show how the system geometry, material properties, and dipole orientations influence the imaging. Further, the near-field interactions among the objects and the imaging element are taken into account and their effects on the image quality are assessed. Our work constitutes fundamental research; the results aid in the development of superlenses and also facilitate in designing superlens imaging setups. A minor topic of this thesis is optical cloaking. In Publication V we consider cloaking from a new perspective: using optical scattering theory we study weakly scattering stratified objects and show that they can be cloaked by suitable slab structures.

The main points of this thesis are to assess the resolution of superlenses, as defined by dipolar point objects, and to evaluate the effects of dipole interactions on near-field imaging. Therefore I begin by introducing in Chapter 2 the theory of electric point dipoles, which I also use to describe nanoscale scatterers. Chapter 3 then contains the methods for evaluating the dipole field on both sides of the slab structures. In Chapter 4, I discuss the optical properties of metals and metamaterials, and give a review on the progress on metamaterials. Chapter 5 contains the theoretical background and recalls the development of the near-field superlenses. This chapter also includes a summary of our research on the near-field imaging with superlenses that is reported in Publications I–IV. Since optical cloaking is a secondary topic of this thesis I discuss it separately after superlens imaging. More specifically, in Chapter 6 I first give an overview of cloaking with various methods including transformation optics. Then I introduce the elements of electromagnetic scattering theory, and summarize

our work on cloaking with weak scatterers that is reported in Publication V. The main conclusions and future prospects of superlens imaging and cloaking are discussed in Chapter 7. The Maxwell equations, the basic theory of electromagnetic optics, and the main mathematical tools that we use are outlined in Appendix A.

2. Electric point dipole

In classical electromagnetic optics small scatterers, such as atoms, molecules, or nanoparticles, are often treated as electric point dipoles [10, 12]. In Publications I–IV we study the near-field imaging of dipole-like nanoobjects with metallic and metamaterial superlenses. This chapter introduces how the characteristic properties of dipolar emitters, e.g., dipole moment, polarizability, and electric field, can be calculated.

2.1 Point-dipole radiation

The electromagnetic field generated by a point dipole is conventionally deduced using the theory of Green's functions as described in App. A.4. In a linear, isotropic, stationary, homogeneous, and spatially nondispersive medium the electric field at a point $\mathbf{r}$ generated by an arbitrarily oriented dipole, having the dipole moment $\mathbf{q}$ and located at $\mathbf{r}_0$, takes the form [10]

$$\mathbf{E}(\mathbf{r},\omega) = \mu\omega^2 \overleftrightarrow{\mathbf{G}}(\mathbf{r},\mathbf{r}_0,\omega)\mathbf{q}, \tag{2.1}$$

where μ denotes the magnetic permeability of the medium and ω is the angular frequency. The Green function, $\overleftrightarrow{\mathbf{G}}(\mathbf{r},\mathbf{r}_0,\omega)$, is a second-rank tensor and the dipole moment is a vector quantity with Cartesian components q_x, q_y, and q_z. The dyadic, outgoing (time-dependence $e^{-\mathrm{i}\omega t}$), free-space Green function has an expression [10, 25]

$$\overleftrightarrow{\mathbf{G}}(\mathbf{r},\mathbf{r}_0,\omega) = \left[\overleftrightarrow{\mathbf{I}} + \frac{1}{k^2}\nabla\nabla\right] G(\mathbf{r},\mathbf{r}_0,\omega), \tag{2.2}$$

where $\overleftrightarrow{\mathbf{I}}$ is the unit dyad, k is the wave number, and $G(\mathbf{r},\mathbf{r}_0,\omega)$ denotes the scalar free-space Green function [10, 25]

$$G(\mathbf{r},\mathbf{r}_0,\omega) = \frac{e^{\mathrm{i}k|\mathbf{r}-\mathbf{r}_0|}}{4\pi|\mathbf{r}-\mathbf{r}_0|}. \tag{2.3}$$

Inserting the scalar Green function into Eq. (2.2), one finds the Green tensor in the Cartesian system [10]

$$\overleftrightarrow{\mathbf{G}}(\mathbf{r},\mathbf{r}_0,\omega)=\left[\left(1+\frac{\mathrm{i}}{kR}-\frac{1}{k^2R^2}\right)\overleftrightarrow{\mathbf{I}}+\left(-1-\frac{3\mathrm{i}}{kR}+\frac{3}{k^2R^2}\right)\frac{\mathbf{RR}}{R^2}\right]\frac{e^{\mathrm{i}kR}}{4\pi R}, \quad (2.4)$$

where $R=|\mathbf{R}|=|\mathbf{r}-\mathbf{r}_0|$ and $\mathbf{RR}$ denotes the vector outer product.

The Green tensor in Eq. (2.4) defines a symmetric 3×3 matrix which, together with Eq. (2.1), specifies the electric field of an electric dipole. The Green tensor contains three different terms according to its R dependence. In the far field, for which $R\gg\lambda$, only the terms with $(kR)^{-1}$ survive. On the other hand, in the near field ($R\ll\lambda$) the terms with $(kR)^{-3}$ give the major contribution, whereas the intermediate field ($R\approx\lambda$) is dominated by the terms with $(kR)^{-2}$.

2.2 Effective polarizability of a dipolar emitter

An effective polarizability is often introduced to take into account the interaction of a single dipolar particle with its environment. The interaction results from the fact that the emitted dipole field scatters back from the inhomogeneities of the environment and influences the dipole properties. The dipole moment of a polarizable particle located at $\mathbf{r}=\mathbf{r}_0$ is related to the total exciting field $\mathbf{E}_{\mathrm{ex,tot}}$ at the dipole site as [10]

$$\mathbf{q}=\overleftrightarrow{\alpha}(\omega)\mathbf{E}_{\mathrm{ex,tot}}(\mathbf{r}_0,\omega), \quad (2.5)$$

where $\overleftrightarrow{\alpha}$ is the polarizability tensor of the emitter. The field $\mathbf{E}_{\mathrm{ex,tot}}$ can be divided into two contributions:

$$\mathbf{E}_{\mathrm{ex,tot}}(\mathbf{r}_0,\omega)=\mathbf{E}_{\mathrm{ex}}(\mathbf{r}_0,\omega)+\mathbf{E}_{\mathrm{ds}}(\mathbf{r}_0,\omega), \quad (2.6)$$

with $\mathbf{E}_{\mathrm{ex}}$ being an external exiting field that is also present in the absence of the particle, and $\mathbf{E}_{\mathrm{ds}}$ is the dipole's field scattered back to its position. Consequently, Eq. (2.5) takes the form

$$\mathbf{q}-\overleftrightarrow{\alpha}(\omega)\mu\omega^2\overleftrightarrow{\mathbf{G}}_{\mathrm{s}}(\mathbf{r}_0,\mathbf{r}_0,\omega)\mathbf{q}=\overleftrightarrow{\alpha}(\omega)\mathbf{E}_{\mathrm{ex}}(\mathbf{r}_0,\omega), \quad (2.7)$$

where $\overleftrightarrow{\mathbf{G}}_{\mathrm{s}}$ is the Green tensor which accounts for the scattering from the environment. One may note that, unlike $\overleftrightarrow{\mathbf{G}}$ in Eqs. (2.1)–(2.4), $\overleftrightarrow{\mathbf{G}}_{\mathrm{s}}$ has no singularity at the dipole site. By defining the effective polarizability $\overleftrightarrow{\alpha}_{\mathrm{eff}}$ for the system one can calculate the dipole moment as

$$\mathbf{q}=\overleftrightarrow{\alpha}_{\mathrm{eff}}(\omega)\mathbf{E}_{\mathrm{ex}}(\mathbf{r}_0,\omega), \quad (2.8)$$

with

$$\overleftrightarrow{\alpha}_{\mathrm{eff}}(\omega) = \overleftrightarrow{\alpha}(\omega)[\overleftrightarrow{\mathbf{I}} - \overleftrightarrow{\alpha}(\omega)\mu\omega^2\overleftrightarrow{\mathbf{G}}_{\mathrm{s}}(\mathbf{r}_0, \mathbf{r}_0, \omega)]^{-1}. \tag{2.9}$$

The effective polarizability contains both the information of the optical properties of the environment which are included in $\overleftrightarrow{\mathbf{G}}_{\mathrm{s}}$ and the properties of the particle itself that are described by the polarizability $\overleftrightarrow{\alpha}$. Irrespective of the environment a particle also creates a field in its own location, which has an impact on the polarizability. This effect, known as the radiation reaction, thus is separate from the influence of the environment. It is addressed in the next section.

In Publications I and II we use a radiating electric dipole as an object for superlens imaging. We do not take into account the interaction between the emitter and the lens, and thus, the electric field of the dipole is calculated simply by using Eq. (2.1). In contrast, in Publication III we study the superlens imaging of a point-like emitter that is excited by a plane wave and which interacts with the lens. In that case the exciting field $\mathbf{E}_{\mathrm{ex}}$ consists of the illuminating plane wave and the part of this plane wave that is reflected back from the lens, whereas $\overleftrightarrow{\mathbf{G}}_{\mathrm{s}}$ corresponds to the Green tensor for the dipole-field reflection from the superlens.

2.3 Polarizability of a small particle

In near-field optics nanoparticles are usually considered as small spheres and their polarizabilities are taken to be isotropic [10, 12]:

$$\overleftrightarrow{\alpha}(\omega) = \alpha(\omega)\overleftrightarrow{\mathbf{I}}, \tag{2.10}$$

with α being a scalar polarizability. The simplest, and consequently widely used way to calculate the electromagnetic response of such a sphere is to use the polarizability given by the Clausius–Mossotti relation [10, 26]

$$\alpha_{\mathrm{CM}}(\omega) = 4\pi\epsilon_0\epsilon_{\mathrm{rm}}(\omega)a^3\frac{\epsilon_{\mathrm{rs}}(\omega) - \epsilon_{\mathrm{rm}}(\omega)}{\epsilon_{\mathrm{rs}}(\omega) + 2\epsilon_{\mathrm{rm}}(\omega)}, \tag{2.11}$$

where a is the radius of the sphere and ϵ_0 is the dielectric permittivity of vacuum. The parameters ϵ_{rm} and ϵ_{rs} denote the relative dielectric permittivities of surrounding medium and the sphere, respectively.

The Clausius–Mossotti result is the polarizability of a small sphere in a uniform and static electric field. When a particle is placed in a time-varying electric field an oscillating dipole is created which produces electromagnetic radiation. This radiation not only dissipates the energy of the

external field but it also influences the motion of the charge in the particle. The effect is known as the radiation reaction or radiation damping and it causes a k^3-dependent correction term in the polarizability [27]

$$\alpha_{\rm rr}(\omega) = \frac{\alpha_{\rm CM}(\omega)}{1 - {\rm i}(k^3/6\pi\epsilon_0)\alpha_{\rm CM}(\omega)}. \tag{2.12}$$

The radiative reaction correction applies to any oscillating dipole, be it an elementary molecular dipole or the dipole induced in a small nanoparticle.

In Publications I–IV we consider the imaging of point dipoles characterizing molecule-like objects for which we take $\alpha \approx 1 \cdot 10^{-30}$ Cm^2/V consistently with typical atomic dipole moments and unit-amplitude incident electric field [28]. In Publication IV we also use as objects glass and metal nanospheres and calculate their polarizabilities using Eq. (2.11). We do not take into account the radiation reaction because the effect amounts only a small correction to the polarizability.

2.4 Coupled dipole method

When a system consists of N individual nanoscatterers each of these can be considered as a point dipole [10]. These dipoles are connected via their fields and one needs to find out the total electric field that excites a given scatterer. This method is known as the coupled dipole method (CDM) and it is widely used in nanooptics [10, 12]. For instance in near-field imaging techniques one employs this approach for analyzing the interaction of a sample and the detector [12, 29, 30]. CDM is also the basis for the discrete dipole approximation (DDA) in which the optical properties of larger particles are studied by dividing them into smaller dipolar subvolumes [31–36].

Let us consider an object consisting of N coupled dipolar emitters for which the location of the nth emitter is denoted by $\mathbf{r}_n$. The total electric field produced by the system, $\mathbf{E}_{\rm tot}$, at a point $\mathbf{r}$ outside the particles is [10]

$$\mathbf{E}_{\rm tot}(\mathbf{r},\omega) = \mathbf{E}_{\rm ex}(\mathbf{r},\omega) + \mu\omega^2 \sum_{n=1}^{N} \overleftrightarrow{\mathbf{G}}(\mathbf{r},\mathbf{r}_n,\omega)\mathbf{q}_n, \tag{2.13}$$

where $\mathbf{E}_{\rm ex}$ is an exciting field which is also present in the absence of particles. The dipole moment of the nth emitter can be calculated by Eq. (2.5), but now the total exciting field includes also the fields radiated by the other particles:

$$\mathbf{q}_n = \overleftrightarrow{\alpha}_n(\omega)\mathbf{E}_{\rm ex,tot}(\mathbf{r}_n,\omega), \tag{2.14}$$

where

$$\mathbf{E}_{\mathrm{ex,tot}}(\mathbf{r}_n,\omega) = \mathbf{E}_{\mathrm{ex}}(\mathbf{r}_n,\omega) + \mu\omega^2[\overleftrightarrow{\mathbf{G}}_{\mathrm{s}}(\mathbf{r}_n,\mathbf{r}_n,\omega)\mathbf{q}_n + \sum_{\substack{k=1\\k\neq n}}^{N} \overleftrightarrow{\mathbf{G}}(\mathbf{r}_n,\mathbf{r}_k,\omega)\mathbf{q}_k + \sum_{\substack{k=1\\k\neq n}}^{N} \overleftrightarrow{\mathbf{G}}_{\mathrm{s}}(\mathbf{r}_n,\mathbf{r}_k,\omega)\mathbf{q}_k]. \tag{2.15}$$

The idea of the coupled dipole method in the case of two dipolar particles is illustrated in Fig. 2.1. The quantities $\overleftrightarrow{\mathbf{G}}$ and $\overleftrightarrow{\mathbf{G}}_{\mathrm{s}}$ obey the reciprocity theorem for Green tensors [25, 37]. Combining Eqs. (2.14) and (2.15) one obtains N coupled equations from which the dipole moments for each emitter can be solved numerically. Once the dipole moments are known, the electric field outside the particles can be calculated using Eq. (2.13).

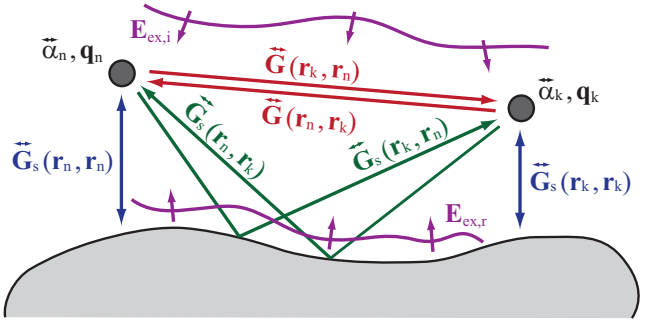

Figure 2.1. Coupled dipole method for two particles. Excited dipolar emitters interact with each other and with the environment. The exciting field $\mathbf{E}_{\mathrm{ex}}$ consists of the incident field $\mathbf{E}_{\mathrm{ex,i}}$ and the part of the incident field that is reflected from the environment $\mathbf{E}_{\mathrm{ex,r}}$.

In Publication IV we study the imaging of two coupled dipole objects with superlenses. In that case we solve two coupled equations to obtain the dipole moments. The total exciting field at the position of each dipole is calculated as a sum of five different fields: the exciting plane wave, the part of the exciting plane wave that is reflected from the lens, the dipole field itself scattered back from the lens, the field of the adjacent emitter, and the field of the adjacent emitter that is reflected from the lens.

3. Electric field of a point dipole in a three-layer structure

For many purposes in optics it is convenient to express fields by employing the angular spectrum representation, i.e., a superposition of plane waves (see App. A.6) [37–39]. We use this approach in Publications I–IV for the calculation of the electric field, produced by a point source, on both sides of the superlens structures. This method is also employed in Publication V where we develop an arbitrary electromagnetic field as a composition of plane waves. This chapter summarizes the steps for expressing the electric field of a point dipole in terms of the angular spectrum representation.

3.1 Angular spectrum representation of dipole field

The diverging scalar spherical wave in Eq. (2.3) can be written using the Weyl representation [38]

$$\frac{e^{\mathrm{i}kR}}{R} = \frac{\mathrm{i}}{2\pi}\iint_{-\infty}^{\infty}\frac{1}{k_z}e^{\mathrm{i}[k_x(x-x_0)+k_y(y-y_0)+k_z|z-z_0|]}\mathrm{d}k_x\mathrm{d}k_y, \tag{3.1}$$

which gives the field in the half-spaces $z \leq z_0$ and $z \geq z_0$ as an angular spectrum of plane waves. The components of the wave vector are denoted by k_x, k_y, and k_z in Eq. (3.1). This expression contains both the propagating waves ($k_z = +[k^2 - (k_x^2 + k_y^2)]^{1/2},\ \ k_x^2 + k_y^2 \leq k^2$) and the evanescent waves ($k_z = +\mathrm{i}[(k_x^2 + k_y^2) - k^2]^{1/2},\ \ k_x^2 + k_y^2 > k^2$). In an absorbing material, the wave vector is always complex and I speak of slowly decaying and fast decaying waves when we refer the waves related to the low and the high spatial frequencies, respectively (see App. A6).

Next, I define two vector triads $(\hat{\mathbf{s}}, \hat{\mathbf{k}}_+, \hat{\mathbf{p}}_+)$ and $(\hat{\mathbf{s}}, \hat{\mathbf{k}}_-, \hat{\mathbf{p}}_-)$ depicted in Fig. 3.1. The vectors $\hat{\mathbf{k}}_\pm$ point in the propagation direction of a plane wave, whereas the vectors $\hat{\mathbf{s}}$ and $\hat{\mathbf{p}}_\pm$ specify the directions of the s-polarized and p-polarized electric field components associated with the plane waves. The plus signs denote the plane waves propagating into the half-space $z \geq z_0$,

and the minus signs refer to those propagating into the half-space $z \leq z_0$. The vector triads satisfy the relation [40]

$$\hat{\mathbf{s}} \times \hat{\mathbf{k}}_\pm = \hat{\mathbf{p}}_\pm, \tag{3.2}$$

with

$$\hat{\mathbf{s}} = \hat{\mathbf{k}}_\parallel \times \hat{\mathbf{u}}_z, \tag{3.3}$$

$$\hat{\mathbf{k}}_\parallel = \mathbf{k}_\parallel / \sqrt{k_x^2 + k_y^2}, \tag{3.4}$$

$$\mathbf{k}_\parallel = k_x \hat{\mathbf{u}}_x + k_y \hat{\mathbf{u}}_y, \tag{3.5}$$

$$\hat{\mathbf{k}}_\pm = \mathbf{k}_\pm / k, \tag{3.6}$$

where $\mathbf{k}_\pm = \mathbf{k}_\parallel \pm k_z \hat{\mathbf{u}}_z$ and $\hat{\mathbf{u}}_x, \hat{\mathbf{u}}_y, \hat{\mathbf{u}}_z$ denote the unit vectors in the Cartesian system. The z axis, representing the main direction of propagation, and the vector $\mathbf{k}_\parallel$ specify the plane of incidence which determines the s and p polarizations. I note that the vector triads defined by Eqs. (3.2)–(3.6) are orthogonal and right-handed but $\hat{\mathbf{k}}_\pm$, and thus also $\hat{\mathbf{p}}_\pm$, are not normalized in the sense of complex-valued vectors [41].

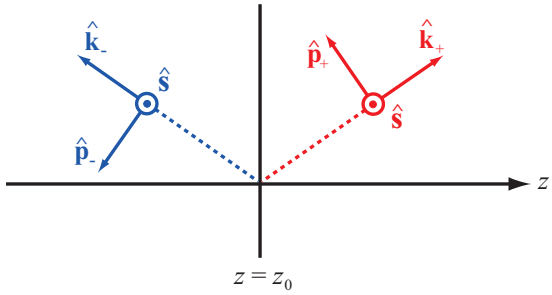

Figure 3.1. Illustration of the orthogonal, right-handed vector triads $(\hat{\mathbf{s}}, \hat{\mathbf{k}}_\pm, \hat{\mathbf{p}}_\pm)$ in the Cartesian coordinate system. The plus signs denote the plane wave propagating into the half-space $z \geq z_0$, whereas the minus signs refer to the propagation into the half-space $z \leq z_0$.

After substitution of the Weyl representation into Eq. (2.2) and some algebraic manipulation the Green tensor takes the form

$$\overleftrightarrow{\mathbf{G}}(\mathbf{r}, \mathbf{r}_0, \omega) = \frac{\mathrm{i}}{8\pi^2} \iint_{-\infty}^{\infty} \frac{1}{k_z} (\hat{\mathbf{s}}\hat{\mathbf{s}} + \hat{\mathbf{p}}_\pm \hat{\mathbf{p}}_\pm)\, e^{\mathrm{i}[\mathbf{k}_\parallel \cdot (\mathbf{r}_\parallel - \mathbf{r}_{\parallel,0}) \pm k_z (z - z_0)]} \mathrm{d}k_x \mathrm{d}k_y, \tag{3.7}$$

where $\mathbf{r}_\parallel = (x, y)$ and $\mathbf{r}_{\parallel,0} = (x_0, y_0)$. Consequently, the dipole electric field can be written as

$$\mathbf{E}(\mathbf{r}, \omega) = \frac{\mathrm{i}\mu\omega^2}{8\pi^2} \iint_{-\infty}^{\infty} \frac{1}{k_z} (\hat{\mathbf{s}}\hat{\mathbf{s}} + \hat{\mathbf{p}}_\pm \hat{\mathbf{p}}_\pm) \cdot \mathbf{q}\, e^{\mathrm{i}[\mathbf{k}_\parallel \cdot (\mathbf{r}_\parallel - \mathbf{r}_{\parallel,0}) \pm k_z (z - z_0)]} \mathrm{d}k_x \mathrm{d}k_y. \tag{3.8}$$

With this equation the dipole field is expressed as a superposition of electromagnetic plane waves which propagate in various directions specified

by $\mathbf{k}_\pm = (\mathbf{k}_\parallel, \pm k_z)$, and whose s- and p-polarized amplitudes are proportional to $\hat{\mathbf{s}} \cdot \mathbf{q}$ and $\hat{\mathbf{p}}_\pm \cdot \mathbf{q}$, respectively. It follows that a dipole aligned along the z axis ($\mathbf{q} \propto \hat{\mathbf{u}}_z$) creates no s-polarized components.

3.2 Reflection and transmission coefficients for a three-layer structure

The superlens geometries analyzed in Publications I–IV are three-layer slab structures. To calculate the dipole field transmitted through and reflected from the lens, one needs to define the transmission and reflection coefficients for the geometry. In this section, I introduce two different ways for doing that.

3.2.1 Boundary condition method

One way to obtain the reflection and transmission coefficients for a three-layer structure is to use the electromagnetic boundary conditions (see App. A.7). In this approach, the first medium contains an incoming plane wave and a wave reflected from the structure. Correspondingly, in the second medium there exist two waves with one propagating in each direction, whereas in the third medium there is only one wave moving away from the second boundary. The detailed derivation of the transmission and reflection coefficients from the boundary conditions is given in Publication III, and the idea is illustrated in Fig. 3.2.

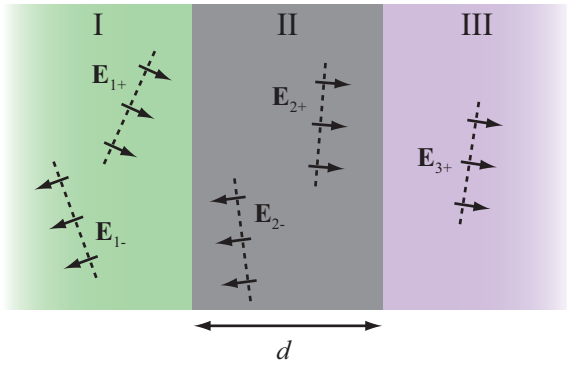

Figure 3.2. Boundary condition method: the plane waves propagate in each medium and the amplitude ratios are calculated using the boundary conditions at the front and rear interface of medium II.

The plane waves in different layers are expressed in terms of s-polarized and p-polarized components using the vector base defined in Sec. 3.1, and

referred to a common origin. Then, the boundary conditions are applied at both interfaces which enable the calculation of the ratios between the amplitudes of the reflected and the incident field ($R_{\mathrm{s,p}} = E^{\mathrm{s,p}}_{1-}/E^{\mathrm{s,p}}_{1+}$), as well as between the transmitted and the incident field ($T_{\mathrm{s,p}} = E^{\mathrm{s,p}}_{3+}/E^{\mathrm{s,p}}_{1+}$). Consequently, one obtains

$$R_{\mathrm{s,p}} = r^{\mathrm{s,p}}_{12} + r^{\mathrm{s,p}}_{23} t^{\mathrm{s,p}}_{12} t^{\mathrm{s,p}}_{21} e^{2\mathrm{i}k_{z2}d}/(1 - r^{\mathrm{s,p}}_{21} r^{\mathrm{s,p}}_{23} e^{2\mathrm{i}k_{z2}d}), \tag{3.9}$$

$$T_{\mathrm{s,p}} = t^{\mathrm{s,p}}_{12} t^{\mathrm{s,p}}_{23} e^{\mathrm{i}k_{z2}d} e^{-\mathrm{i}k_{z3}d}/(1 - r^{\mathrm{s,p}}_{21} r^{\mathrm{s,p}}_{23} e^{2\mathrm{i}k_{z2}d}), \tag{3.10}$$

where $t^{\mathrm{s,p}}_{ij}$ and $r^{\mathrm{s,p}}_{ij}$ denote, respectively, the Fresnel transmission and reflection coefficients for a single interface separating the media i and j, with $i, j = (1, 2, 3)$ (see App. A.8). In addition, $k_{z2} = k'_{z2} + \mathrm{i}k''_{z2}$ is the z component of the wave vector in the absorbing medium II, with $k'_{z2} > 0$, $k''_{z2} > 0$ for conventional (positive-index) media, and $k'_{z2} < 0$, $k''_{z2} > 0$ in the case of negative-index materials. The choice of the sign for the z component of the wave vector is described in Publication I. The procedure does not require the knowledge of the fields in medium II and is valid for both slowly decaying (propagating) and fast decaying (evanescent) waves, as it is a direct consequence of Maxwell's equations.

3.2.2 Partial-wave summation method

The reflection and transmission of plane waves by a three-layer structure can also be treated by partial-wave summation. In this approach, one considers the propagation of each plane-wave component of the dipole field separately and employs a superposition principle. This procedure is described in Publication I and the idea is illustrated in Fig. 3.3.

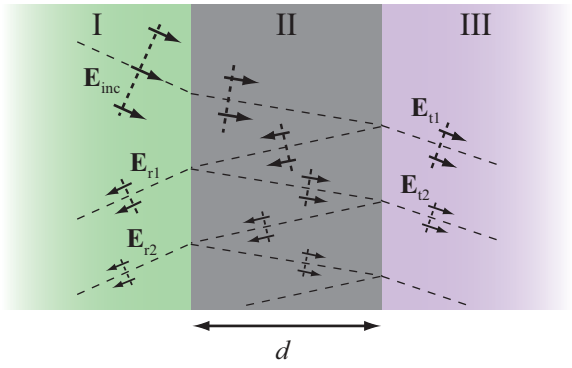

Figure 3.3. Principle of the partial-wave summation method: each plane wave component is multiply reflected in a three-layer structure and the partial waves are summed up at the front and rear interface of medium II.

The transmission and reflection of a single plane wave at each interface of the structure can be treated by using the Fresnel coefficients. One takes also into account the multiple reflections and related propagations inside the slab and sums all the multiply reflected waves at the front or rear interface of medium II. The summation leads to a geometric series for which the condition of convergence is satisfied in the case of the slowly decaying (propagating, low spatial-frequency) waves, in absorbing negative-index and positive-index slab materials. The convergence condition may fail with the fast decaying (evanescent, high spatial-frequency) waves for both types of materials, but the summing of such divergent series is conventionally justified in terms of the analytic continuation [42–44]. By carrying out the summations, one ends up exactly with the same transmission and reflection coefficients for the slab, Eqs. (3.9)–(3.10), as employing the boundary conditions. However, I want to emphasize that with the boundary conditions no argument of analytic continuation is required.

3.3 Green's tensors for reflection and transmission

To deduce the electric field of a point dipole on both sides of the three-layer structure one needs to derive the Green tensors for the reflection and transmission. Using the reflection coefficients for the structure the reflection Green tensor at a point $\mathbf{r} = (x, y, z)$ in medium I ($z < 0$) takes the form

$$\overleftrightarrow{\mathbf{G}}_{\mathrm{r}}(\mathbf{r}, \mathbf{r}_0, \omega) = \frac{\mathrm{i}}{8\pi^2} \int_0^\infty \frac{k_\parallel}{k_{z1}} e^{-\mathrm{i}k_{z1}(z+z_0)} (R_{\mathrm{s}} \overleftrightarrow{\mathbf{S}}_{\mathrm{r}} + R_{\mathrm{p}} \overleftrightarrow{\mathbf{P}}_{\mathrm{r}}) \mathrm{d}k_\parallel. \tag{3.11}$$

The derivation of $\overleftrightarrow{\mathbf{G}}_{\mathrm{r}}$ and the elements of the tensors $\overleftrightarrow{\mathbf{S}}_{\mathrm{r}}$ and $\overleftrightarrow{\mathbf{P}}_{\mathrm{r}}$ can be found in Publication III. Similarly, the transmission Green tensor at a point $\mathbf{r} = (x, y, z)$ in medium III ($z > d$) can be written

$$\overleftrightarrow{\mathbf{G}}_{\mathrm{t}}(\mathbf{r}, \mathbf{r}_0, \omega) = \frac{\mathrm{i}}{8\pi^2} \int_0^\infty \frac{k_\parallel}{k_{z1}} e^{-\mathrm{i}k_{z1}z_0} e^{\mathrm{i}k_{z3}z} (T_{\mathrm{s}} \overleftrightarrow{\mathbf{S}}_{\mathrm{t}} + T_{\mathrm{p}} \overleftrightarrow{\mathbf{P}}_{\mathrm{t}}) \mathrm{d}k_\parallel. \tag{3.12}$$

The derivation of $\overleftrightarrow{\mathbf{G}}_{\mathrm{t}}$ is given in Publication I and the elements for the tensors $\overleftrightarrow{\mathbf{S}}_{\mathrm{t}}$ and $\overleftrightarrow{\mathbf{P}}_{\mathrm{t}}$ are listed in Publications I and III. The use of Eqs. (3.11) and (3.12) in the expressions for the dipole field presented in Chap. 2 enables an efficient numerical calculation of the electric field for a point dipole at the two sides of a three-layer structure.

4. Optical properties of superlens materials

The electric permittivity and the magnetic permeability are the two fundamental parameters characterizing the electromagnetic properties of a medium. In Publications I–IV we use either a silver or a slightly absorbing metamaterial slab as the imaging element of the superlens structures. This Chapter deals with the optical properties of these materials: the electromagnetic response is specified and resulting phenomena, which are important for our studies, are described. I also give an overview on the progress of the present metamaterial designs and discuss briefly the applications of metamaterials.

4.1 Metals

The optical properties of metals have been discussed by many authors [10,45]. I follow a classical picture describing the light-metal interactions.

4.1.1 Electromagnetic response of metals

The optical properties of metals are mainly due to the response of the free conduction electrons to light. A simple way to describe the response of the free electrons to an electromagnetic field is the Drude model [10, 45]. According to this model the relative dielectric permittivity of a metal takes the form [10]

$$\epsilon_{\mathrm{r,Drude}}(\omega) = \epsilon_{\mathrm{r}}' + \mathrm{i}\epsilon_{\mathrm{r}}'' = 1 - \frac{\omega_{\mathrm{p}}^2}{\omega^2 + \Gamma^2} + \mathrm{i}\frac{\Gamma\omega_{\mathrm{p}}^2}{\omega(\omega^2 + \Gamma^2)}, \tag{4.1}$$

where ϵ_{r}' and ϵ_{r}'' represent the real and the imaginary part of the permittivity, respectively, and Γ is a damping constant due to scattering processes of electrons. The quantity $\omega_{\mathrm{p}} = (Ne^2/m_e\epsilon_0)^{1/2}$ is known as the volume plasma frequency, with e being the electron charge, N the number of electrons per unit volume, and m_e the effective mass of electrons. Metals do

not have magnetic response at the optical frequencies, i.e., $\mu_\mathrm{r} = 1$.

From Eq. (4.1) it is seen that ϵ'_r is negative when $\omega^2 < \omega_\mathrm{p}^2$, but still $\omega^2 \gg \Gamma^2$, which is usually the case at optical frequencies [45]. For instance, gold has $\omega_\mathrm{p} = 13.8 \cdot 10^{15}$ s^{-1} and $\Gamma = 1.075 \cdot 10^{14}$ s^{-1} making the real part of the permittivity negative over the visible range [10]. The negative value of ϵ'_r reflects the fact that the electrons oscillate out of phase by π radians with the exciting field [10,45]. The negative real part of permittivity leads to a large imaginary part of refractive index ($n = \sqrt{\epsilon_\mathrm{r}}$), which makes the metal highly reflective [45]. The imaginary part of the refractive index, and consequently the reflectivity, becomes high also when ϵ''_r is large which is the case for sufficiently low values of ω (in the infrared regime). On the other hand, when $\omega^2 > \omega_\mathrm{p}^2$ (but $\omega^2 \gg \Gamma^2$) the real part of the permittivity is positive and ϵ''_r is small compared to ϵ'_r. Thus, the metal behaves essentially as a dielectric material. The Drude model is sufficiently accurate at the infrared frequencies and consequently widely used in optics. However, it needs to be supplemented in the visible regime by the influence of the bound electrons which results in the dielectric constant to exhibit a resonant behavior [10].

Most metals, and especially noble metals, indeed possess a negative real part of the permittivity at the optical frequencies. Widely used values for noble metals are the ones retrieved experimentally by Johnson and Christy [46]. One may note that these are the bulk values which are valid as long as the dimensions of the metal structures are larger than the electron mean free path (~ 10 nm in silver) [10]. When considering nanometer-scale metal films or very small metal nanoparticles the size corrections to the bulk values need to be taken into account [47]. In Publications II–IV we study the near-field imaging with silver superlenses having the silver layer thickness varying from 15 nm to 50 nm, and in line with few recent superlens experiments [14,15], we use the bulk value ($\epsilon_\mathrm{r} = -2.4 + \mathrm{i}0.2$ at $\lambda = 365$ nm [46]) for the silver permittivity.

4.1.2 Surface plasmons

Among the most fascinating consequences of the interaction of metal nanostructures with light is the possibility to excite plasmons [10,48,49]. Plasmons localized in more dimensions than one can be excited in metallic particles, nanowires, or other nanostructures [48–52]. These local surface plasmons are different from surface plasmon polaritons [53,54]. Surface plasmon polaritons are surface-charge-density oscillations that may exist

at the interface of two media having dielectric constants of opposite signs. Research in the field of optics making use of plasmons is mostly concerned with the control of optical radiation on the subwavelength scale [55–58]. This field has progressed rapidly during the recent years and developed into a research area of its own known as plasmonics [59, 60].

I first consider a single planar interface between two materials. The first medium is characterized by its complex, frequency-dependent dielectric permittivity $\epsilon_{\mathrm{r}1} = \epsilon'_{\mathrm{r}1} + \mathrm{i}\epsilon''_{\mathrm{r}1}$, while the second one is a dielectric material having real permittivity $\epsilon_{\mathrm{r}2}$. Using a plane wave approach and applying the electromagnetic boundary conditions at the interface one can find solutions of the Maxwell equations which are localized at the boundary: field modes that propagate along the interface and decay exponentially orthogonal to it. Surface plasmon polaritons of this kind are generated by the surface plasmons and in non-magnetic materials ($\mu_{\mathrm{r}1} = \mu_{\mathrm{r}2} = 1$) these fields are purely p-polarized. The existence conditions and the characteristic properties, such as the propagation distance and the decay length on both sides of the interface, of surface plasmon fields are derived in many textbooks [10, 48, 49]. Surface plasmon polaritons can exist if the real parts of the permittivities of the two media possess opposite signs. Metals, especially noble metals, have negative real part and sufficiently small imaginary part at optical frequencies, and thus interfaces between metals and dielectrics can support polaritons. Surface plasmon polaritons can only be excited by an external field whose wave vector component along the interface is larger than the free-space wave number. Therefore polaritons are normally created by employing gratings or total internal reflection (evanescent wave) in prisms [52].

Surface plasmons can also be excited on the boundaries of a metal film embedded between dielectric media. Well-known experimental arrangements are the Otto and Kretschmann configurations in which an evanescent wave generated by total internal reflection excites polaritons on the surface of a thin metal layer. The existence of the surface plasmons in these setups is manifested by the minimum of the reflected illumination as the energy is transferred to the polariton. At the same time, the intensity of the electric field on the metal surface representing the polariton is strongly enhanced [10, 49]. This corresponds to a near-singularity of the transmission (and reflection) coefficient from the evanescent wave in the metal film to the polariton field. In the three-layer structures of metallic superlenses similar phenomena take place. High spatial-frequency com-

ponents of the field generated by the object are coupled into the metal layer and enhanced by surface plasmons on both interfaces.

In Publications II–IV we consider a thin silver layer as the near-field imaging element. The operation of the silver lens is based on the electric field enhancement of the p-polarized evanescent wave components of the dipole radiation on the metal boundaries due to the excitation of surface plasmons.

4.2 Metamaterials

During the last ten years there has been a strong interest in novel optical media called metamaterials [2–6]. Metamaterials are artificially engineered structures possessing extraordinary physical properties, unavailable in naturally occurring materials, when interacting with an electromagnetic field. The rapid progress in this field has offered an entirely new route to design material properties at will.

4.2.1 Material parameters of metamaterials

An illustrative way to represent the electromagnetic properties of all materials is to use 'a material parameter space' shown in Fig. 4.1 [61]. In this picture, quadrant I contains materials with positive permittivity and permeability, i.e., most dielectric materials. Region II covers metals, ferroelectric materials, and doped semiconductors which can have negative permittivity at certain frequencies. Quadrant IV is composed of few ferrite materials having negative permeability at some frequencies [61]. However, this kind of magnetic response fades away above the microwave frequencies and in the optical regime $\mu_{\mathrm{r}} = 1$ holds for all naturally existing materials [62]. Region III embraces metamaterials for which the permeability and the permittivity are simultaneously negative, but in nature, materials of this type do not exist. Metamaterials consist of periodically or randomly structured sub-units whose size and separation are much smaller than the wavelength of an electromagnetic field. Consequently, microscopic details of individual structure elements can not be sensed by the field, but the average of the assembly's collective response matters. The electromagnetic response of this kind of material can be characterized by an effective relative permittivity $\epsilon_{\mathrm{r,eff}}$ and permeability $\mu_{\mathrm{r,eff}}$. What makes the metamaterials attractive is the fact that the effective perme-

ability can have non-unity and even negative values at the optical wavelengths. In addition, the effective material parameters can be controlled using properly designed structures.

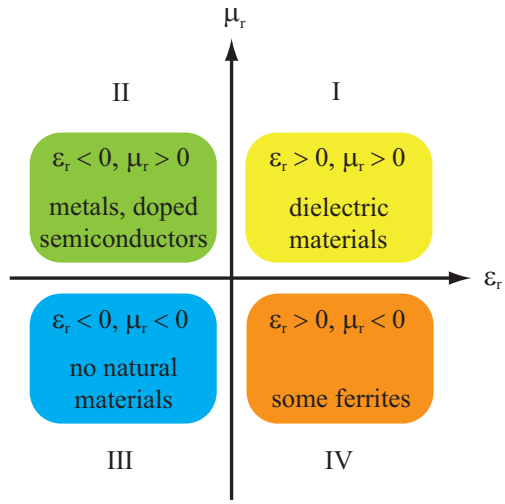

Figure 4.1. Material parameter space described by the relative electric permittivity ϵ_r and the relative magnetic permeability μ_r [61].

Various theoretical models for the effective material parameters have been developed during the past decade [63–67]. However, it is often very difficult to derive analytical formulas for the effective parameters of certain metamaterials due to the complexity of the structure. Alternatively one may retrieve the effective parameters from numerical simulations [68, 69]. Very recently, the theory of effective material parameters was questioned because it does not take into account the non-local effects (spatial dipersion) in the present metamaterial designs [70].

My focus is not in the rather challenging research dealing with the analytical quantification of material parameters for a certain metastructure. Instead, I analyze the superlens imaging problem and take a metamaterial slab, having negative effective material parameters, both as a generalization of Pendry's perfect lens and as a reference for a silver slab structure.

4.2.2 Structure and progress of metamaterial designs

Artificial magnetic response of metamaterials can be achieved, for instance, by loop-like resonant structures made of conducting materials. In 1999, John Pendry proposed a design, known as split ring resonators

(SRR), for obtaining negative magnetic permeability [63]. The route to manufacture metamaterials with a negative effective refractive index is to combine two sets of structures with $\mathrm{Re}(\epsilon_{\mathrm{r,eff}}) < 0$ and $\mathrm{Re}(\mu_{\mathrm{r,eff}}) < 0$ in the same frequency range. This kind of structure, operating at the microwave frequencies and consisting of copper SRRs and wires, was first experimentally demonstrated in 2000 [64]. After that several SRR-based metamaterial designs have been advanced from microwave frequencies to the optical regime by scaling down the structure size [71–76]. However, it was found that the magnetic response of SRRs decreases with the downscaling of the structure, and negative values of the permeability can not be reached at the visible region [77, 78].

Another proposed metamaterial design is a nanorod structure for which negative refractive index is reported at telecommunication wavelengths and even in the red part of the visible spectrum [79–82]. The most successful optical NIM structure so far is the fishnet structure which has recently brought the negative refractive index from the infrared regime to the visible wavelengths and enabled the fabrication of bulk metamaterials [83–88]. One of the major challenges of optical NIMs based on resonant structures is the strong energy dissipation of the electromagnetic field. A possible way of addressing this issue is to incorporate gain media into NIM designs [89, 90]. An alternative route towards the NIMs is the to use chiral materials [91–94]. Negative refraction is also demonstrated in semiconductor metamaterials [95].

The amount of losses in NIMs is often described by the figure of merit ($\mathrm{FOM} = -\mathrm{Re}(n)/\mathrm{Im}(n)$). The most promising optical NIM designs proposed so far are a low-loss bulk NIM (FOM 3.5) working at near-visible wavelengths [86], a loss-free and active NIM operating in the red part of the visible spectrum [90], and a bistable and self-tunable NIM structure (FOM 8.5) working at $\lambda = 650$ nm [96].

4.2.3 Electromagnetic properties of NIMs

The idea of NIMs was actually born in the early 20th century among the works on a negative phase velocity and its consequences [4]. Later, in the forties and fifties the optical properties of NIMs were studied by Russian physicists [4]. The most well known step was made by Veselago in 1967 with a systematic study on the electromagnetic properties of materials having negative material parameters [1]. However, at that time no materials were available for testing Veselago's ideas and they remained as a

scientific curiosity until Pendry inspired the recent boom on NIMs [63].

Veselago considered monochromatic plane waves in a lossless medium having real and negative permittivity and permeability. Starting from the Maxwell equations he showed that the wave vector $\mathbf{k}$, the electric field $\mathbf{E}$, and the magnetic field $\mathbf{H}$ of a plane wave form a left-handed triad in medium with $\epsilon_r < 0, \mu_r < 0$, whereas in a normal medium the triplet is right-handed. Due to this property materials with simultaneoustly negative permittivity and permeability are called left-handed materials (LHMs). Moreover, the Poynting vector defined as $\mathbf{S} = \mathbf{E} \times \mathbf{H}$ is antiparallel to the wave vector $\mathbf{k}$ in LHMs. It was also proven that the refractive index given by $n = \pm\sqrt{\epsilon_r \mu_r}$ must take the negative value which is the reason for the often used term negative-index materials. Veselago further pointed out that if light is incident from a positive-index material to a NIM, the refracted light lies on the same side as the incident one with respect to the surface normal - the effect known as negative refraction. These phenomena are illustrated in Fig. 4.2. In addition, Veselago showed that the Doppler effect and the Cherenkov effect are reversed in NIMs [1].

In Publications I, III, and IV we consider slightly absorbing metamaterial, having $\epsilon_r = \epsilon_r' + i\epsilon_r''$ and $\mu_r = \mu_r' + i\mu_r''$, with $\epsilon_r', \mu_r' < 0$ and ϵ_r'', μ_r'' being small positive numbers, as a superlens material. For our studies, an im-

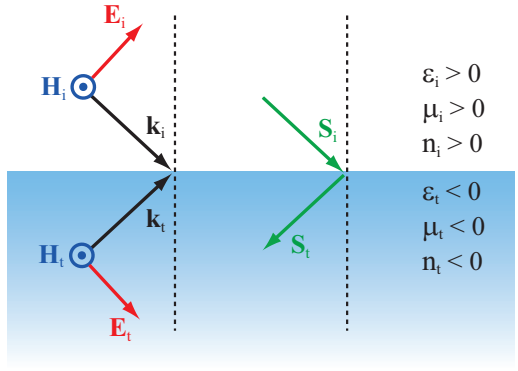

Figure 4.2. Illustration of the counterintuitive electromagnetic properties of negative-index materials proposed by Veselago [1]. The subscript i denote the medium of incidence (conventional, positive-index material) and t the medium of transmittance (NIM). The wave vector $\mathbf{k}$, the electric field $\mathbf{E}$, and the magnetic field $\mathbf{H}$ of a plane wave constitute a left-handed triad in NIMs, whereas in conventional materials the triplet is right-handed. Negative refraction takes place at the interface of positive and negative-index materials. The wave vector $\mathbf{k}$ and the Poynting vector $\mathbf{S}$ are antiparallel in NIMs, while in positive-index materials they are parallel.

portant consequence of the negative $\epsilon'_{\rm r}$ and $\mu'_{\rm r}$ is the fact that the sign of the real part of wave vector's z-component (the component along the propagation direction) is reversed: $k_{z,2} = k'_{z,2} + {\rm i}k''_{z,2}$, with $k'_{z,2} < 0$, $k''_{z,2} > 0$. This result is derived in Publication I using the theory of complex functions, in a manner following an earlier study [97]. Another remarkable point to notice is the magnetic response ($\mu_{\rm r} \neq 1$) of our NIM lens material. As mentioned in Sec. 4.1.2 the fields generated by the surface plasmons are purely p-polarized which results from the absence of the magnetic response of metals at the optical range. If the material has a negative real part of the permeability, plasmon-like magnetic resonances can occur for s-polarized light as well [52]. This effect leads to a greater enhancement of the evanescent wave components of the object radiation in transmission through a metamaterial slab than through a silver slab in which only the p-polarized waves are amplified.

4.2.4 Applications of metamaterials

Due to their unusual properties metamaterials have a number of potential uses. At microwave frequencies metamaterials have already been employed in various applications, such as magnetic resonance imaging [98], compact waveguides [99], novel microwave circuits [100], and microwave antennas [101]. One attractive metamaterial device is the perfect lens providing an image resolution beyond the diffraction limit [13]. The concept of perfect lens (superlens) has been demonstrated experimentally at microwave, mid-infrared, and optical frequencies [7]. Another hot topic within the metamaterial community is the control of the flow of light in desirable manners which enables, for instance, to design cloaking devices making objects invisible or less detectable [8, 9]. Further, tunable metamaterials can be used for modulating and switching EM waves at terahertz frequencies [102]. An interesting application of metamaterials are also perfect absorbers making the individual absorption of the electric and magnetic components of EM waves possible [103].

As mentioned before, this thesis concerns two applications of metamaterials: Publications I–IV focus on the superlenses, whereas Publication V deals with optical cloaking. The principles and our main results related to these topics are introduced in the following two chapters.

5. Near-field imaging with slab superlenses

Most of this thesis is focused on near-field imaging of dipole-like objects with silver and slightly absorbing NIM superlenses. In this chapter, I first introduce the concepts for defining the resolution of an imaging system. Then, I show how the perfect lens and its physical realizations, known as superlenses, work as an imaging device. I also give an overview on the recent development on near-field superlenses. The last section summarizes the research reported in Publications I–IV.

5.1 Resolution in far-field imaging

Spatial resolution is a measure of the capability to distinguish two separated objects. The diffraction limit states that the resolution in optical imaging is limited by the wavelength of light and the numerical aperture (NA) of the instrument. However, the near-field imaging techniques allow us to access the evanescent wave components of the object radiation which effectively increase the NA and leads to spatial resolutions beyond the diffraction limit [10, 12].

5.1.1 Point-spread function

The point-spread function (PSF) defines the resolution of an optical imaging system. The image of a radiating point source appears to have a finite size, and as the name indicates, PSF describes the spread of the field created by a point source in an imaging process. This broadening is a consequence of spatial filtering: a point source in space is characterized by a delta function and its radiation embraces the infinite spectrum of spatial frequencies, but on propagation from the object to the image, high-spatial-frequency components (evanescent waves) are filtered out. In addition, all propagating waves cannot either be collected due to the finite size of the

lenses which leads to a further reduction in bandwidth. With the reduced spectrum of the object radiation a part of information is lost in the imaging process and a complete reconstruction of the original point source in the image is not possible.

The classic theory of diffraction of electromagnetic fields by optical systems is that of Richards and Wolf [104]. The smallest radiating electromagnetic unit is a point dipole, and as discussed in Chap. 2, most subwavelength-sized particles scatter as electric dipoles in the optical regime. The imaging of a dipole by aplanatic lens systems (obeying the sine condition [105]), in which the distance between the object and the image is much larger than the wavelength of light, has been analyzed by many authors [10, 106, 107]. The quantity $|\mathbf{E}|^2$, where $\mathbf{E}$ is the dipole field in the image region, is often used to denote the point-spread function since it is relevant to optical detectors. If the optical axis of such systems is along the z direction, the transverse PSF is calculated in the image plane as $|\mathbf{E}(x, y, z = \text{constant})|^2$ (see Fig. 5.1). For dipoles aligned perpendicular to the axis the distribution of $|\mathbf{E}|^2$ in paraxial approximation is slightly broader in the direction of the dipole than orthogonal to it, in excellent agreement with the exact calculation [10]. The characteristic widths of these profiles specify the size Δr of the PSF. In contrast, the field strength along the optical axis in the image area, calculated as $|\mathbf{E}(x = 0, y = 0, z)|^2$, gives the axial PSF (see Fig. 5.1). Its characteristic width Δz gives the depth of field. The quantities Δr and Δz depend on both the magnification (M) and the numerical aperture (NA) of the imaging system. As an example, for a typical microscope objective with $M = 60$ and $\text{NA} = 1.4$, and for wavelength $\lambda = 500$ nm, one obtains $\Delta r \approx 13\ \mu$m and $\Delta z \approx 1.8$ mm [10].

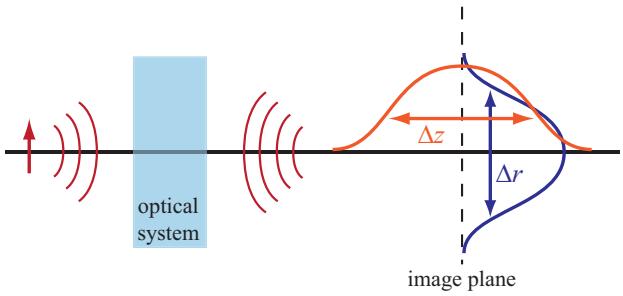

Figure 5.1. Illustration of the transverse (blue curve) and axial (orange curve) point-spread functions (PSFs) characterized by the widths Δr and Δz, respectively. In electromagnetic imaging the transverse width depends on the direction in the image plane and the orientation of the object dipole.

In electromagnetic imaging the PSF depends strongly on the orientation of the dipole. In conventional far-field systems the image has a clear peak-shaped profile if the dipole is oriented perpendicular to the optical axis. On the other hand, for a dipole aligned along the axis, the image-intensity distribution is zero on the optical axis and contains two peaks on both sides of the axis. In the latter case it is more difficult to define the characteristic width of the transverse PSF. The image of a dipole along optical axis is a bit wider than the image of a dipole oriented perpendicular to the axis [10]. The situation is different in near-field imaging with slab lenses, as will be seen in Sec. 5.4.

5.1.2 Diffraction limit

Now, as we have seen how a single point-like object is mapped to the image, our next task is to define how two point dipoles that are separated by a distance $\Delta r_{\parallel} = [(\Delta x)^2 + (\Delta y)^2]^{1/2}$ can be distinguished. When moving two point emitters in the object plane closer to each other, their PSFs in the image start to overlap. At some point, two emitters become indistinguishable. If the point sources are uncorrelated one can view them as resolvable if the maxima of their PSFs in the image are separated by more than the characteristic width of one individual PSF. Accordingly, a narrow PSF leads to a better resolution than a wider one.

As mentioned in the last section, the resolving capability of an imaging system depends on the bandwidth of spatial frequencies that are collected by the system:

$$\Delta k_{\parallel} = [(\Delta k_x)^2 + (\Delta k_y)^2]^{1/2}. \tag{5.1}$$

Straightforward Fourier analysis leads to a relation [37, 108]

$$\Delta k_{\parallel} \Delta r_{\parallel} \geq 1, \tag{5.2}$$

where $\Delta k_{\parallel}$ and $\Delta r_{\parallel}$ are the rms widths and $\Delta r_{\parallel}$ gives the minimum resolvable separation in the object plane. In far-field imaging only propagating waves are collected: the upper bound for $\Delta k_{\parallel}$ is defined by the wave number $k = 2\pi n/\lambda$, with n being the refractive index of the medium in which the object is located. Thus, the minimum for the spatial resolution is

$$\mathrm{Min}[\Delta r_{\parallel}] = \frac{\lambda}{2\pi n}. \tag{5.3}$$

However, the entire spectrum of propagating waves cannot be collected and the resolution limit is affected by the NA of the imaging system.

The theoretical limit for the resolution of a microscope is often taken to follow Abbe's or Rayleigh's early works [45]. Both Abbe and Rayleigh state that two point-like objects are distinguished if the maximum of one paraxial PSF in the image coincides with the first minimum of the second PSF. In that case, the ratio of the intensity minimum at the midpoint of the image distribution to the intensity maximum is 0.81. This kind of analysis leads to [10, 45]

$$\mathrm{Min}[\Delta \mathrm{r}_{\parallel}]_{\mathrm{Abbe-Rayleigh}} = 0.61\frac{\lambda}{\mathrm{NA}} \approx \frac{\lambda}{2\mathrm{NA}}. \tag{5.4}$$

Abbe's formulation is based on the paraxial approximation and only the special case of two parallel dipoles aligned perpendicular to the optical axis is analyzed [10]. If the dipoles are aligned parallel to the optical axis the definition of the resolution limit becomes somewhat arbitrary due to the shape of the PSFs, as discussed in the previous section.

According to Eq. (5.2) the resolution is unlimited if the bandwidth of the object radiation in the image is arbitrarily large. Going beyond the limit given in Eq. (5.3) requires the detection of the evanescent wave components which is the subject of near-field imaging techniques [10, 12]. Publications I–IV deal with the near-field imaging with the superlenses and the remaining part of this chapter concerns that topic.

5.2 The perfect lens

The idea of the perfect lens was born in Veselago's early studies in 1967 dealing with the electromagnetic properties of NIMs [1]. However, the increased number of works concerning this unconventional lens were not inspired until John Pendry complemented Veselago's ideas in 2000 [13].

5.2.1 Focusing of propagating waves

The perfect lens is a transversally infinite, flat slab of ideal NIM that is surrounded by vacuum. The refractive index of the perfect lens material equals -1 and the lens thickness is d. If an object is located at a distance a ($a < d$) in front of the slab, the image at the distance $d - a$ behind the slab will be perfect. Veselago introduced the idea of the perfect lens using ray optics [1]. He proposed that light rays emerging from the object exhibit negative refraction at the interfaces of the NIM slab. Negative refraction allows the flat slab to focus all the diverging light rays from the point object into a point behind the slab. Other characteristics of the sys-

tem include a double focusing effect – another image is formed inside the slab. The focusing action of the perfect lens is illustrated in Fig. 5.2(a). The relative permittivity and permeability of NIM slab are equal in magnitude but opposite in sign to those of vacuum, i.e., $\epsilon_{r2} = -1$, $\mu_{r2} = -1$, making the Fresnel reflection coefficients zero. Consequently, the interfaces of the lens show no reflection and the light is perfectly transmitted through it. However, one may note that the perfect lens is not a lens in the conventional sense of the word since it can not focus normally incident light.

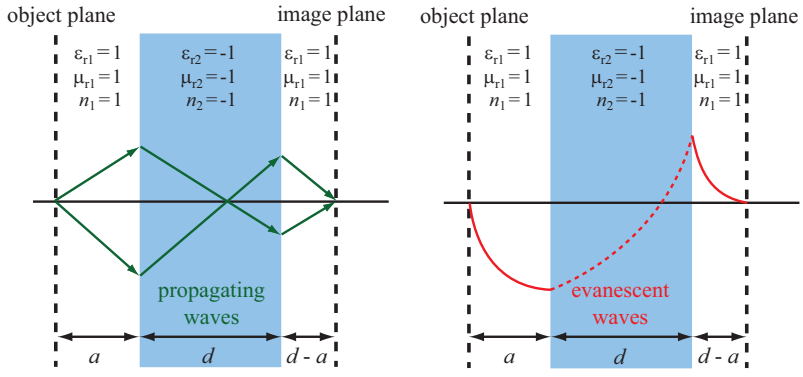

Figure 5.2. Transversally infinite flat slab acts as the perfect lens. The thickness of the slab is d, the refractive index equals -1, and the slab is surrounded by vacuum. The slab (a) brings all propagating light rays from the object plane into a focused image, and (b) enhances the evanescent waves so that the net amplitude change between the object and image plane is zero (red dashed line, see Eq. (5.12)). The increase of the amplitudes takes place at the boundaries due to surface resonances, as discussed in the main text.

In his famous paper, Pendry applied a plane-wave approach to analyze the imaging with the perfect lens [13]. When considering the propagating waves of the object radiation Pendry stated that the transport of energy in the propagation direction of the plane wave ($+z$ direction) implies the conventional choice of the positive sign for the wave vector's z component in vacuum, but in NIM the negative sign for the z component is required:

$$k_{z1} = +\sqrt{\epsilon_{r1}\mu_{r1}k_0^2 - (k_x^2 + k_y^2)}, \quad k_x^2 + k_y^2 \leq \epsilon_{r1}\mu_{r1}k_0^2, \tag{5.5}$$

$$k_{z2} = -\sqrt{\epsilon_{r2}\mu_{r2}k_0^2 - (k_x^2 + k_y^2)}, \quad k_x^2 + k_y^2 \leq \epsilon_{r2}\mu_{r2}k_0^2. \tag{5.6}$$

Here k_0 is the wave number in vacuum, subscript 1 denotes the vacuum (medium I) surrounding the lens and 2 refers to the lens material (medium II). Together with the material parameters $\epsilon_{r1} = \mu_{r1} = 1$ and $\epsilon_{r2} = \mu_{r2} = -1$, Eqs. (5.5) – (5.6) lead to the Fresnel reflection and trans-

mission coefficients that are equal to zero and 1, respectively. Further, the reflection and transmission coefficients of the perfect lens become [13]

$$R_{\mathrm{s,p}} = 0, \tag{5.7}$$

$$T_{\mathrm{s,p}} = e^{\mathrm{i}k_{z2}d} = e^{-\mathrm{i}k_{z1}d}, \tag{5.8}$$

where s and p refer to the s- and p-polarized waves, respectively. From these equations one sees that the lens reflects no light and cancels the phase change of the propagating waves when they travel from the object plane to the front surface of the lens, and again, from the back surface of the lens to the image plane. Thus, Pendry's conclusions concerning the propagating waves match with Veselago's ideas.

5.2.2 Enhancement of evanescent waves

The new message of Pendry's study were his results concerning the evanescent wave components of the object radiation. In contrast to the case of the propagating waves, Pendry chose the same sign for the z components of the wave vector in both media [13]:

$$k_{z1} = +\mathrm{i}\sqrt{k_x^2 + k_y^2 - \epsilon_{\mathrm{r}1}\mu_{\mathrm{r}1}k_0^2}, \quad k_x^2 + k_y^2 > \epsilon_{\mathrm{r}1}\mu_{\mathrm{r}1}k_0^2, \tag{5.9}$$

$$k_{z2} = +\mathrm{i}\sqrt{k_x^2 + k_y^2 - \epsilon_{\mathrm{r}2}\mu_{\mathrm{r}2}k_0^2}, \quad k_x^2 + k_y^2 > \epsilon_{\mathrm{r}2}\mu_{\mathrm{r}2}k_0^2. \tag{5.10}$$

These choices were justified by the fact that the evanescent waves must decay exponentially in both media with increasing z. However, Eqs. (5.9)–(5.10) with the material parameters $\epsilon_{\mathrm{r}1} = \mu_{\mathrm{r}1} = 1$, $\epsilon_{\mathrm{r}2} = \mu_{\mathrm{r}2} = -1$ lead to a diverging Fresnel reflection and transmission coefficients. To avoid this divergence, Pendry derived the reflection and transmission coefficients of the perfect lens using the summation method, introduced in Sec. 3.2.2, in the limit $\epsilon_{\mathrm{r}2}, \mu_{\mathrm{r}2} \to -1$. With this approach one obtains [13]

$$\lim_{\epsilon_{\mathrm{r}2},\mu_{\mathrm{r}2}\to-1} R_{\mathrm{s,p}} = 0, \tag{5.11}$$

$$\lim_{\epsilon_{\mathrm{r}2},\mu_{\mathrm{r}2}\to-1} T_{\mathrm{s,p}} = e^{-\mathrm{i}k_{z2}d} = e^{-\mathrm{i}k_{z1}d}. \tag{5.12}$$

Substitution of Eq. (5.9) into Eq. (5.12) implies that the amplitudes of the evanescent waves increase in the transmission through the slab by the same amount as they decay in free space on both sides of the slab: the net amplitude change between the object plane and the image plane is zero. I emphasize that the evanescent waves are not amplified on propagation within the slab, but the amplitudes change at the boundaries. This extraordinary behavior relies on the fact that NIM supports resonant

surface waves, one example of which are waves due to surface plasmons. The enhancement of evanescent waves in the perfect lens is illustrated in Fig. 5.2(b). Because evanescent waves do not carry any net energy flux, the energy of the field is not increased and only the distribution of the energy across the space, i.e., the energy density, is changed.

In summary, the perfect lens not only cancels the phase change for the propagating waves, but also restores the amplitudes of the evanescent waves which allows the creation of the perfect image with unlimited resolution. However, shortly after its publication Pendry's work aroused a fair amount of debate among the scientists [42,43,109–114]. Without taking side in the arguments I merely consider Pendry's theory as a starting point for a more detailed study of superlenses.

5.3 Imaging with superlenses

Negative-index materials are necessarily dispersive and hence lossy [61]. Accordingly, the material parameters of NIMs must contain the imaginary parts as well, and especially, resonance-based NIMs are inherently associated with considerable energy dissipation. Lenses that take this practical limitation into account are known as superlenses. Despite the rapid progress of NIMs, the realizations of NIM superlenses are few because properly working bulk NIMs are still more or less unattainable with modern fabrication techniques. However, the subwavelength resolution can also be achieved with physically realizable metallic slab lenses [7,13].

5.3.1 Enhancement of evanescent waves

The idea of the metallic superlens was also mentioned in Pendry's paper [13]. One can consider a slab-lens imaging system in the electrostatic (quasi-static) limit when all the dimensions of the system are much smaller than the wavelength of light [13]:

$$\sqrt{k_x^2 + k_y^2} \gg \omega/c_0 = k_0, \tag{5.13}$$

where c_0 is the vacuum speed of light. Now, several formulas concerning the perfect lens can be approximated by taking the limit $k_x^2 + k_y^2 \to \infty$. The z components of the wave vectors take the forms [13]

$$k_{z1} = +\mathrm{i}\sqrt{k_x^2 + k_y^2 - \epsilon_{\mathrm{r}1}\mu_{\mathrm{r}1}k_0^2} \approx +\mathrm{i}\sqrt{k_x^2 + k_y^2}, \quad \text{when } k_x^2 + k_y^2 \gg k_0^2, \tag{5.14}$$

$$k_{z2} = +\mathrm{i}\sqrt{k_x^2 + k_y^2 - \epsilon_{\mathrm{r}2}\mu_{\mathrm{r}2}k_0^2} \approx +\mathrm{i}\sqrt{k_x^2 + k_y^2}, \quad \text{when } k_x^2 + k_y^2 \gg k_0^2, \tag{5.15}$$

i.e., $k_{z2} = k_{z1}$ in this limit. Using these expressions one finds that the transmission coefficient of the slab for p polarization becomes independent of $\mu_{\rm r}$, and if $\epsilon_{\rm r1} = 1$, $\epsilon_{\rm r2} \to -1$, one obtains [13]

$$\lim_{\epsilon_{\rm r2}\to -1} T_{\rm p} = e^{+{\rm i}\sqrt{k_x^2+k_y^2}d}, \quad \text{when } k_x^2 + k_y^2 \gg k_0^2. \tag{5.16}$$

Thus, the p-polarized evanescent wave components of the object radiation can be amplified with a slab lens having negative $\epsilon_{\rm r2}$ only. Similarly, in the quasi-static limit T_s becomes independent of $\epsilon_{\rm r2}$ and a slab with negative permeability ($\mu_{\rm r2} = -\mu_{\rm r1}$) would amplify the s-polarized evanescent waves. The superlens effect therefore remains valid for one polarization in a medium having only one of the material parameters negative. Natural candidates for superlens material in the case of p-polarized light are noble metals, and especially silver, because of its low losses at optical frequencies.

Shortly after the proposal of the superlens, various theoretical studies on superlens properties were published [115–119]. These studies predicted that the subwavelength resolution is achievable with silver superlenses, but only with a carefully chosen design. At first, the distance between the slab and the object and image planes, as well as the slab's thickness must be small compared with the wavelength. In addition, the losses of the lens material need to be small, and a good impedance match (i.e., negligible reflections at the interfaces) between the lens and its environment is required. It appears that the quantities which describe the imaging capability of superlenses are the slab's transmission coefficients. The losses, even very small ones, change the behavior of the slab's transmission coefficients from exponentially growing (see Eqs. (5.12) and (5.16)) to peak-shaped exceeding unity only at a certain range of high spatial frequencies. Consequently, the feature that crucially separates the superlenses from the conventional ones is that the resolution is not limited by diffraction, but rather defined by how much and in how wide a range of spatial frequencies the evanescent waves are enhanced.

5.3.2 Development of near-field superlenses

Pendry's proposal inspired also experimental attempts to test the superlens concept in practice. First, the enhancement of the evanescent waves across the slab was demonstrated [120, 121]. These studies brought out valuable suggestions concerning the slab thickness and surface roughness requirements. During the years 2003 and 2004 the first superlens designs

providing a subwavelength resolution at microwave frequencies were realized [122–124]. In 2005, the superlensing effect was observed in the optical range [14, 15].

Figure 5.3 shows the cross-section of the superlens structure reported in Refs. [14,15]. In that design a thin silver film with the optimized thickness of 35 nm is embedded between two dielectric materials. The first dielectric medium in front of the silver slab is a polymethyl methacrylate (PMMA) spacer layer having the thickness of 40 nm. The second one behind the silver layer is a photoresist (PR) used for recording the image. The object is a 2D chromium grating or an arbitrary 2D object patterned on top of the PMMA spacer. The object is illuminated from behind with a light having $\lambda_0 = 365$ nm (I-line of the mercury lamp). At this wavelength silver shows a negative real part of the permittivity and the impedance match with the dielectrics is good: $\epsilon_{\mathrm{PMMA}} \approx 2.3$, $\epsilon_{\mathrm{Ag}} \approx -2.4 + \mathrm{i}0.2$, and $\epsilon_{\mathrm{PR}} \approx 2.9$ (while $\mu_{\mathrm{PMMA}} = \mu_{\mathrm{Ag}} = \mu_{\mathrm{PR}} = 1$). As a consequence of the enhancement of the evanescent wave components scattered from the object, the subwavelength resolutions of $\lambda_0/6$ [14] and $\lambda_0/7$ [15] were demonstrated. One of the major challenges, limiting the enhancement of the evanescent waves and consequently the attainable resolution with silver superlenses, is the difficulty in manufacturing smooth and flat surfaces. In 2010, an ultra thin and smooth silver superlens was fabricated by employing a new method utilizing Ge-Ag surface interactions [16]. With this design a 2D grating object was imaged with a resolution of $\lambda_0/12$. I also mention that already in 2006, a low-loss SiC superlens based on surface phonons and operating at mid-infrared frequencies (~ 10 μm) was reported to provide a resolution of $\lambda_0/20$ [125].

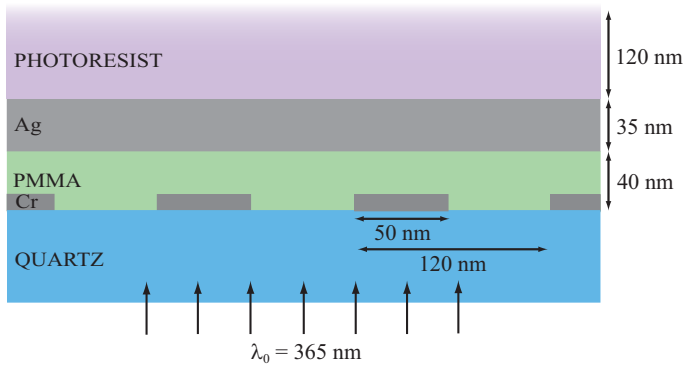

Figure 5.3. Cross-section of a silver superlens structure. The image of 50 nm Cr grating with 120 nm period is resolved in the photoresist providing the resolution of $\lambda_0/7$ [15].

The superlenses discussed so far enable the construction of the image only in the near field because the evanescent waves decay rapidly after the lens. One of the future challenges is to bring the subwavelength image into the far field. This may be possible with the so called far-field superlenses (FSLs) which converts the evanescent waves behind the lens into propagating ones [126], or with cylindrical hyperlenses [127]. There already exist a few demonstrations of such lenses [128, 129]. Although these concepts are very interesting and promising they do not fall within the scope of this thesis.

5.4 Near-field imaging of point-like objects with superlenses

In this section I summarize our research dealing with the near-field imaging of dipolar emitters with NIM and silver superlenses.

5.4.1 Imaging of a radiating dipole with NIM superlens

Publication I is a detailed study concerning electromagnetic imaging with a slightly lossy metamaterial superlens surrounded by vacuum (see Fig. 1 in I). The object is a single radiating point dipole. The material parameters of the lens are close to those of the perfect lens: $\epsilon_{\mathrm{r}2} = -1 + \mathrm{i}\epsilon''$ and $\mu_{\mathrm{r}2} = -1 + \mathrm{i}\mu''$, with ϵ'' and μ'' being small positive numbers. The slab thickness d is few tens of nanometers. The distance between the object plane and the front surface of the slab, as well as between the rear surface of the slab and the image plane are equal to $d/2$, in line with the superlens system.

We first show how the sign of the wave vector in a lossy NIM can be determined. Then, using the angular spectrum representation and the partial-wave summation, we derive the Green tensor for the dipole field transmitted through the slab lens. The Green tensor includes the transmission coefficients of the slab, which describe the quality of the slab as a near-field imaging device. We show how the transmission coefficients behave as a function of spatial frequencies: the absolute values of the coefficients exhibit a peak-shaped behavior and exceed unity at a certain range of the spatial frequencies (see Fig. 4 in I). This enables the enhancement of evanescent wave components of the object radiation, but not over the whole range of spatial frequencies as the perfect lens would do. Consequently, the image of a point source is a spot with a finite size.

When the losses or the slab thickness increase the enhancement range of the evanescent waves moves towards lower spatial frequencies and gets narrower because the absorption in the slab increases.

With the derived formalism we evaluate numerically the point-spread function in the image plane behind the slab, and verify that the NIM slab increases the resolution several orders of magnitude when compared with conventional imaging (see Figs. 5 and 6 in I). The resolution is well beyond the diffraction limit for both the dipole oriented parallel to the slab and orthogonal to the slab. With numerical simulations we also point out that the resolution of the imaging system decreases linearly as a function of d, whereas it depends logarithmically on ϵ'' and μ'' (see Fig. 8 in I).

5.4.2 Imaging of a radiating dipole with silver superlens

In Publication II we extend our formalism, developed in Publication I, to the case of a silver superlens. In this geometry a thin silver film is sandwiched between two dielectrics (see Fig. 1 in II). The first half-space before the silver layer is composed of polymethyl methacrylate (PMMA) and the half-space behind the lens is filled with photoresist (PR). The object plane is located 40 nm in front of the lens and the image is considered immediately (2 nm) behind the lens. Thus, the imaging system is similar to that used in the experiments [14, 15], but our object is a radiating point dipole instead of a two-dimensional grating or structure. The dipole, which is a genuine three-dimensional object since the moment can be arbitrarily oriented, radiates at the wavelength of $\lambda_0 = 365$ nm for which $\epsilon_{\mathrm{PMMA}} \approx 2.3$, $\epsilon_{\mathrm{Ag}} \approx -2.4 + \mathrm{i}0.2$, and $\epsilon_{\mathrm{PR}} \approx 2.9$.

We show that the enhancement of the evanescent waves occurs for p polarization, but not for the s-polarized waves due to the lack of magnetic response (see Fig. 2 in II). The enhancement is not as strong as with the slightly lossy NIM because of higher losses and worse impedance match, and again, the enhancement decreases when the slab thickness is increased. Also in this study, we evaluated the PSFs in the image plane and defined the resolution of the system (see Fig. 3 in II). Now the resolution depends strongly on the orientation of the object dipole. The resolution for the dipole oriented orthogonal to slab is better because the dipole field in that case contains only p-polarized components. In contrast, the field of the dipole aligned parallel to slab contains both polarizations, and the s-polarized near-field components are not enhanced in transmission. We obtained the resolutions $\lambda_0/4$ and $\lambda_0/8$ for the dipoles aligned parallel and

orthogonal to the slab, respectively. In this paper we also show that the quasi-static approximation leads to considerable differences in the behavior of the transmission coefficients for p-polarization, but accurate results on resolution, when compared to the exact calculation.

Figure 5.4 illustrates the superlens effect of the silver slab. In Fig. 5.4(a), the normalized intensity distribution is calculated at the plane $z = 77$ nm in PMMA when the dipole is oriented along the z-axis and located at the origin. The distance of 77 nm is equal to the separation between the object and image planes when a slab of thickness 35 nm is included. Figure 5.4(b) shows the normalized PSF in the image plane of the superlens. When comparing these figures one sees that the silver slab increases the image brightness by several orders of magnitude. In addition, the width of the distribution is more than two times narrower when the slab is present.

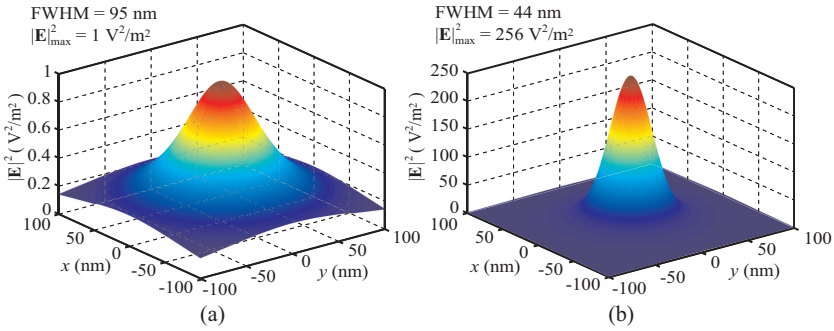

Figure 5.4. Normalized intensity distributions (a) at the plane $z = 77$ nm in PMMA and (b) at the image plane of the silver superlens ($d = 35$ nm) for the object dipole oriented along the z-axis. The dipole is located at the origin and radiates at the wavelength of $\lambda_0 = 365$ nm.

5.4.3 Imaging of a dipole interacting with superlens

The first two publications contain important results on superlens imaging. However, those studies do not take into account interactions between the object and the imaging device, which is an inherent feature in the near-field techniques and may distort the image. In Publication III we take a few steps further towards more physical imaging conditions: we excite a polarizable point object by an external plane wave and include in the analysis the influence of the slab on the dipole radiation.

In Publication III we investigate the near-field interactions of a single polarizable point dipole with a silver and a slightly absorbing NIM slab. Our major goal is to find out how the interactions affect the object emis-

sion and image quality, and could these superlenses be used as a near-field detection device that does not interact with the object. We consider superlenses having geometries similar to those in Publications I–II, but now the object dipole is a scatterer excited by a normally (from behind) or perpendicularly (from below) incident plane wave (see Fig. 1 in III). To investigate the influence of the interactions on imaging we derive the Green tensor for reflection and evaluate the effective polarizability for the dipolar emitter that includes the effect of the slab.

The main result of this paper is that the magnitude of the dipole moment decreases and eventually vanishes when the dipole approaches the imaging slab. This is verified both analytically (see Eq. (30) in III) and numerically (see Figs. 2 and 3 in III). The effect arises from the dipole–slab near-field interaction: for small dipole–slab distances (< 40 nm) the reflected dipole near-field cancels the dipole moment induced by the exciting field. The suppression of the dipole emission occurs for both the silver and NIM lenses, but it is stronger and reaches over the near-field range in the case of silver lens because of stronger reflection. Physically the reflection of the dipole field from the slab can be described by the method of mirror dipole in the quasi-static regime.

We also calculate the image-intensity distributions and show that the interactions decrease the image brightness for both superlenses, and if the object is too close to the slab its image is no longer distinguishable (see Figs. 4, 5, and 6 in III). For instance, in the case of 35 nm thick silver lens the brightness in the observation plane for the dipole–slab separations of 40–50 nm is about 10^3 times higher without the interaction than with it. On the other hand, the image width was found to be the same with and without the dipole–slab interaction. Thus, the slab attenuates the dipolar emission and therefore decreases the image brightness, but the shape of the distribution remains essentially unaffected. We further verified that despite the near-field interaction, a 35 nm thick NIM slab could be used as a non-interacting imaging device if the losses are very low ($\epsilon_{\rm r} = \mu_{\rm r} = -1 + {\rm i}0.001$) and the object–slab distance is larger than 50 nm. As a conclusion, silver and NIM slabs can be used as near-field elements to image a three-dimensional dipole field with subwavelength resolution, but the near-field interactions bring out restrictions for the dipole–slab distance.

5.4.4 Imaging of two interacting dipoles

Publications I–III deal with individual dipoles and the results on resolution are valid when two such objects are uncorrelated. This limitation in removed in Publication IV where we extend our analysis to the superlens imaging of two dipole objects which interact with each other and with the slab. Our aim is to determine how the interactions among the objects and the lens affect the imaging. The imaging geometry corresponds to that in Publication III, but the object plane contains two polarizable point-like scatterers (see Fig. 1 in IV). We consider three types of objects having different polarizabilities, as listed in Table 5.1. For molecule-like objects we take $\alpha = 1 \cdot 10^{-30}$ Cm^2/V consistently with atomic dipole moments and unit-amplitude incident electric field [28]. We also use values $\alpha = 5 \cdot 10^{-33}$ Cm^2/V and $\alpha = 5 \cdot 10^{-35}$ Cm^2/V which, according to the Clausius–Mossotti relation (see Sec. 2.3), characterize the polarizabilities of a metallic sphere of radius $R_\mathrm{s} \sim 20$ nm and a glass sphere of radius $R_\mathrm{s} \sim 10$ nm, respectively. We do not take into account the radiation reaction because the effect amounts only to a negligible correction to the polarizability of the spheres. Using the coupled dipole method, described in Sec. 2.4, we derive the dipole moments for the emitters which include the dipole–dipole and dipole–slab interactions.

Table 5.1. Polarizabilities of various dipolar objects. The abbreviation QM refers to quantum mechanics and CM to the Clausius–Mossotti formulation. The symbol R_s is the radius of a sphere.

object	α [Cm^2/V]	method	size
molecule	$1 \cdot 10^{-30}$	QM	atomic
metal sphere	$5 \cdot 10^{-33}$	CM	$R_\mathrm{s} \sim 10$ nm
glass sphere	$5 \cdot 10^{-35}$	CM	$R_\mathrm{s} \sim 20$ nm

To analyze the interactions we calculated the magnitudes of the dipole moment components as a function of their distance from the slab and from each other (see Fig. 2 in IV). The dipole–slab near-field interactions manifest themselves in a similar manner as reported in Publication III. The dipole–dipole interactions also suppress the emission of the dipoles and the effect depends on the polarizabilty of the objects. If two metallic or glass nanospheres are not placed in contact to each other (i.e., $\Delta x > 3R_\mathrm{s}$) or close to a silver or NIM slab (i.e., $|z_0| > 3R_\mathrm{s}$), the object–object and object–slab near-field interactions do not influence radically the emission

strength of the objects. However, if two molecules of high polarizability are brought to within the near-field distances from each other ($\Delta x < \lambda_1/2$, where λ_1 is the wavelength in medium I) or the imaging slab ($|z_0| < \lambda_1/2$), the suppression of the emission is significant.

In fact, we found that the dipole–dipole interactions cause an interesting and unexpected phenomenon: if two point dipoles are placed very close to each other their dipole moments die out. This is a consequence of the direct near-field interaction of the adjacent dipoles. The same phenomenon appears also in many earlier studies, but the vanishing of the dipole moments is conventionally avoided by considering small nanospheres which cannot be closer to each other than $2R_s$ [29,31,34]. However, for point-like emitters this somewhat unphysical behavior exists which raises doubts about the validity of the dipole approximation. Within nano-scale distances particles interact with each other and the environment through their evanescent fields and the quadrupole interactions may became significant [10]. Due to their difficulty, these higher-order interactions are very rarely included in the analysis. It is also pointed out that for dielectric spheres whose radius is smaller than 50 nm the inclusion of the quadrupole interaction leads to results which are very close to those of the CDM at optical frequencies [130]. One needs also to remember that a point dipole, with zero size and infinite field strength in its origin, is itself an unphysical element and may cause these apparently counterintuitive phenomena. Thus, when evaluating the image-intensity distributions and the resolution of the imaging system (within the dipole approximation) we place neither the molecular emitters nor the nanospheres in contact with each other.

By calculating the PSFs we found that the interference of two point-like objects aligned parallel to the slab makes the image intensity profiles obscure with multiple maxima. Consequently, unlike with uncorrelated dipoles, subwavelength near-field imaging of two correlated point-like emitters is impossible if the objects are excited in such a way that their dipole moments are predominantly parallel to the surface of the imaging element. However, when the objects are aligned orthogonally to the slab, the interference does not disturb the imaging as much: two clear intensity peaks form in the observation plane and their positions match with the object locations in the object plane (see Fig. 3 in IV). In the latter case we find the resolutions of $\sim \lambda_1/5$ and $\sim \lambda_1/10$ for the silver and slightly lossy metamaterial superlens structures, respectively (see Fig. 4

in IV). We also propose that such a near-field imaging arrangement can in practice be created through excitation by total internal reflection illustrated schematically in Fig. 5.5 (see also Fig. 5 in IV).

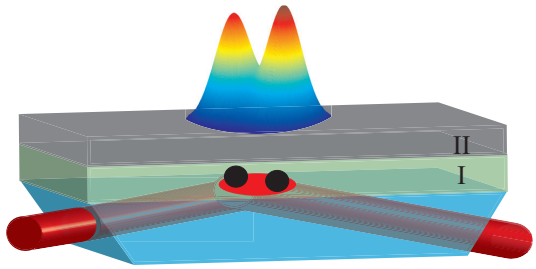

Figure 5.5. Schematic illustration of an object excitation with a prism. The exciting field in medium I is an evanescent wave traveling along the interface and decaying orthogonal to it. Its electric field component is effectively orthogonal to the surface of the imaging element (medium II), as shown in Publication IV.

6. Optical cloaking

Another, a bit smaller topic of this thesis is optical cloaking. That subject has received the attention of scientists during the last six years, and especially, making an object invisible or less detectable with the methods of transformation optics is widely studied [8, 9]. In Publication V we approach invisibility cloaking by a different route: we present a cloaking based on the classical scattering theory with weak slab scatterers. In this Chapter, I first give an insight into the cloaking by means of transformation optics and describe other cloaking approaches. Then, I introduce the basic elements of electromagnetic scattering, and finally, summarize the research reported in Publication V.

6.1 Survey of optical cloaking

It is a well-known phenomenon in optics that a light ray undergoes refraction at the interface of two media. A common example of this is a lens in which the light feels a change of the refractive index in the air-glass interfaces. If the refractive index varies continuously in the medium, the refraction of the light ray is continual and the ray trajectory is a smooth curve. In 2006, two independent studies by Ulf Leonhardt and John Pendry suggested that using the transformation optics it is possible to make an invisibility cloak that guides light around a region in space [17, 18]. An artificially engineered cloaking shell curves the incident light rays [17] or wave fronts [18] around an object after which the light continues traveling along its original direction on the opposite side of the object. Consequently, it looks like there is nothing on the path of the wave and the observer sees the empty space behind the object. The idea is illustrated in Fig. 6.1. These reports triggered an explosively increased number of studies in the field of optical cloaking [8, 9].

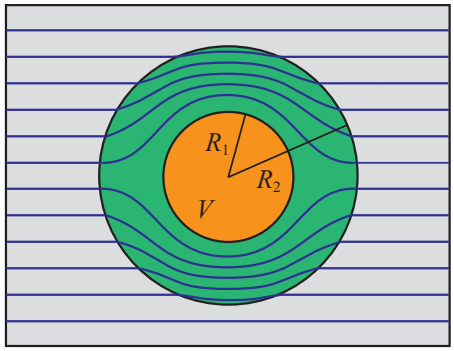

Figure 6.1. Cross-section of a spherical cloak. The object is located in the region V ($r < R_1$), while the space $R_1 < r < R_2$ is occupied by the cloaking material. The light rays striking the system circulate around V and are squeezed into the cloaking shell. On the other side of the system, the rays continue their propagation undeviated from their original course [18].

The idea of cloaking based on coordinate transformation relies on the invariance of the Maxwell equations [18]. In this approach the field lines (normal to the wavefronts) are modified by a specified cloak to avoid a given region V, where an object is placed. The light rays incident onto V are squeezed into the cloak, while the rays outside the cloak are unaffected. No light penetrates into or escapes from the region V amounting to what is known as 'blind cloaking'. Due to their invariance, the Maxwell equations retain their form in the coordinate transformation and the procedure yields the required permittivity and permeability of the cloaking medium. In an alternative approach one uses the technique of conformal mapping to define a refractive index distribution that guides light rays around the object region V [17, 131].

The spherical cloak shown in Fig. 6.1 does not require negative material parameters, but ϵ_r and μ_r in the cloak shell need to be smaller than unity and perfect cloaking is achieved only at a single frequency. After the pioneering works [17, 18], many authors have followed the technique of coordinate transformation and proposed cloaks having different forms and shapes [132–134]. These cloaks normally require highly anisotropic materials having extreme values of ϵ_r and μ_r, which implies narrow operation bandwidth and high losses. However, the first cloaking device operating over a band of microwave frequencies has proved the principles of cloaking [19]. It is built of ten cylindrical layers of split-ring resonators (SRR) and the experiments show that the cloak decreases significantly scattering by the object and reduces its shadow.

Another cloaking technique, having its roots in transformation optics

and highly promising to mitigate the disadvantages of earlier designs, is the carpet cloak [135]. Such structures have been experimentally demonstrated at microwave frequencies [136] and in the optical range [20, 21]. For instance, a particular carpet cloak involving isotropic dielectric material renders a remarkable suppression of scattering from a μm-sized object within a broad band of near-infrared frequencies [20]. Quite recently, a quasi-three-dimensional optical carpet cloak that decreased significantly the scattering from an object for viewing angles up to 60°, was fabricated [22].

Besides the cloak designs based on coordinate transformations and conformal mappings, a variety of other cloaking approaches and related methods have been put forward. These include reduction of scattering cross-section [137, 138], use of embedded arrays of holes and dielectric particles in metal films [139], and utilization of anomalous resonances [140]. For specific light polarizations even mm- and cm-scale three-dimensional objects are cloaked in visible light [141]. Most of these techniques are approximate, narrow-band, or based on strong scatterers. Some cloaking methods can be categorized as 'cloaking at distance'. In such a case an invisibility cloak can hide an object that is external to the cloak itself. The cloak, which depends on the object, typically is designed employing the concept of complementary media [142].

6.2 Optical scattering theory

In general, scattering covers a wide range of phenomena arising from the interaction of waves or particles with media. We focus on the circumstances where the response of matter to an electromagnetic field can be described by the macroscopic material parameters and assume that the properties of the scattering medium do not change in time. Let us consider a monochromatic electromagnetic field that propagates in vacuum and is incident on a medium occupying a volume V (see Fig. 6.2). The medium is characterized by the dielectric permittivity $\epsilon_{\rm r}$ and the magnetic permeability $\mu_{\rm r}$, and it contains no sources of electromagnetic field. In this case the wave equation in Eq. (A.17) (see also App. A.5) takes the form

$$\nabla \times \nabla \times \mathbf{E}(\mathbf{r},\omega) - k^2(\mathbf{r},\omega)\mathbf{E}(\mathbf{r},\omega) = 0, \tag{6.1}$$

where $k^2 = k_0^2 n^2(\mathbf{r},\omega) = k_0^2 \epsilon_{\rm r}(\mathbf{r},\omega)\mu_{\rm r}(\mathbf{r},\omega)$, with k_0 being the vacuum wave number and n the refractive index. Using vector identities, Maxwell's

equations, and the constitutive relations, Eq. (6.1) can be expressed as

$$\nabla^2\mathbf{E}(\mathbf{r},\omega)+\nabla\left[\left(\frac{\nabla\epsilon_{\rm r}(\mathbf{r},\omega)}{\epsilon_{\rm r}(\mathbf{r},\omega)}\right)\cdot\mathbf{E}(\mathbf{r},\omega)\right]+k^2(\mathbf{r},\omega)\mathbf{E}(\mathbf{r},\omega)=0. \tag{6.2}$$

This equation is valid in any nanophotonic structure as long as it can be described by macroscopic material parameters. The middle term on the left-hand side in Eq. (6.2) couples the three orthogonal components of the electric field.

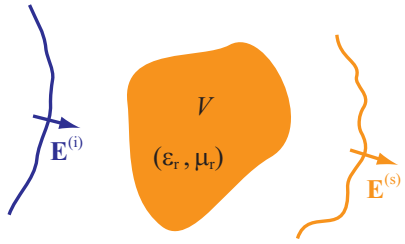

Figure 6.2. Electromagnetic field is incident on and scattered from a medium occupying a volume V and characterized by the dielectric permittivity $\epsilon_{\rm r}$ and the magnetic permeability $\mu_{\rm r}$.

We now assume that the material properties within V vary smoothly with position. If $\epsilon_{\rm r}$ changes so slowly that it is effectively constant over distances of the order of the wavelength, i.e., $|\nabla\epsilon_{\rm r}|\lambda\ll\epsilon_{\rm r}$, the middle term on the left-hand side of Eq. (6.2) is negligible in comparison with the first one [45, 143]. We then obtain

$$\nabla^2\mathbf{E}(\mathbf{r},\omega)+k_0^2n^2(\mathbf{r},\omega)\mathbf{E}(\mathbf{r},\omega)=0, \tag{6.3}$$

indicating that the electric field components are decoupled. Hence, under these conditions scalar theory of optical scattering is sufficient.

Denoting the scalar field by $U(\mathbf{r},\omega)$ Eq. (6.3) can be rewritten as [45]

$$\nabla^2U(\mathbf{r},\omega)+k_0^2U(\mathbf{r},\omega)=-4\pi F(\mathbf{r},\omega)U(\mathbf{r},\omega), \tag{6.4}$$

where

$$F(\mathbf{r},\omega)=\frac{1}{4\pi}k_0^2[n^2(\mathbf{r},\omega)-1] \tag{6.5}$$

is the scattering potential of the medium. The function F vanishes outside the scattering volume V. The field U can always be expressed as a sum $U=U^{(\rm i)}+U^{(\rm s)}$, where $U^{(\rm i)}$ satisfies Eq. (6.4) with $F=0$. The field $U^{(\rm i)}$ is thus generated by sources at infinity and it can be viewed as the incident field, whereas $U^{(\rm s)}$ may be regarded as the scattered field (see Fig. 6.2). The solution of Eq. (6.4) is [45] (cf., App. A.4)

$$U(\mathbf{r},\omega)=U^{(\rm i)}(\mathbf{r},\omega)+\int_V F(\mathbf{r}',\omega)U(\mathbf{r}',\omega)\frac{e^{{\rm i}k_0|\mathbf{r}-\mathbf{r}'|}}{|\mathbf{r}-\mathbf{r}'|}{\rm d}^3r', \tag{6.6}$$

where the last term under the integral is the outgoing free-space Green function. Equation (6.6) is the integral equation of potential scattering; it is an integral equation for $U^{(\mathrm{s})}$ within the volume V.

According to Eq. (6.6) one can calculate the total field outside the scatterer if $U^{(\mathrm{s})}$ in V is known. However, in many practical situations finding the exact $U^{(\mathrm{s})}$ may be difficult and one has to resort to approximate techniques. In the case of a weak scatterer, whose refractive index according to Eq. (6.5) is close to that of the surroundings, the total field within the scatterer can be approximated by the incident field only. Thus, Eq. (6.6) becomes [45]

$$U(\mathbf{r},\omega) = U^{(\mathrm{i})}(\mathbf{r},\omega) + \int_V F(\mathbf{r}',\omega) U^{(\mathrm{i})}(\mathbf{r}',\omega) \frac{e^{\mathrm{i}k_0|\mathbf{r}-\mathbf{r}'|}}{|\mathbf{r}-\mathbf{r}'|} \mathrm{d}^3 r'. \tag{6.7}$$

This expression, which is the first term in an iterative series solution for the scattering problem, is the (first-order) Born approximation. Despite its simplicity the Born approximation gives reasonable results in many cases of optical scattering.

6.3 Cloaking in the Born approximation

In Publication V we study cloaking by means of classical scattering theory in the case of weak slab scatterers. We consider a monochromatic field $U^{(\mathrm{i})}(\mathbf{r},\omega)$ propagating in vacuum along the z axis and striking a slab object, as illustrated in Fig. 6.3 (also Fig. 1 in V). The object is located between $0 \leq z \leq a$ and it has a z-dependent refractive-index distribution $n_{\mathrm{o}}(z,\omega)$. The cloak slab is placed at $a_1 \leq z \leq a_2$, where $a_1 > a$. Our goal is to determine the refractive index $n_{\mathrm{c}}(z,\omega)$ for the cloak such that the field $U_{\mathrm{c}}(\mathbf{r},\omega)$ scattered from it cancels exactly the scattered field $U_{\mathrm{o}}(\mathbf{r},\omega)$ produced by the known object. The refractive-index distributions of the object and the cloak are taken smooth and their contrast with the surroundings low so that the scalar treatment under the first-order Born approximation is valid. We therefore consider an object-dependent cloak and the process can be classified as cloaking at distance.

We express the incident and scattered fields by means of the angular spectrum representation presented in App. A.6. Cloaking is achieved when the fields scattered by the object and the cloak cancel each other, i.e., $U_{\mathrm{o}} = -U_{\mathrm{c}}$, implying that the total field in the space behind the cloak or in front of the object is equal to the incident field. The former is referred to as forward cloaking and the latter as backward cloaking, and they place

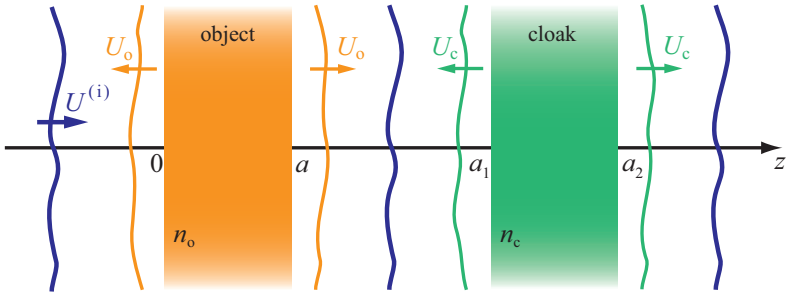

Figure 6.3. Illustration of cloaking in a slab geometry. The field $U^{(i)}$ propagates along the z axis in vacuum and is incident on the object (n_o, $0 \le z \le a$) and cloak (n_c, $a_1 \le z \le a_2$) slabs. The fields scattered by the object and cloak are denoted by U_o and U_c, respectively.

different conditions on the scattering potential of the cloak. These cloaking conditions enable us to derive the required refractive-index distribution for the cloak slab. For simplicity, the thicknesses of the object and cloak slabs are taken to be equal.

We show that in the forward direction (observer in the half-space $z > a_2$) any absorbing, stratified, and weakly scattering object can be cloaked by a slab consisting either of amplifying (active) ordinary medium or of negatively refractive, absorbing metamaterial. Under the conditions assumed the cloaking is perfect, occurs for any incident field at all frequencies, and is independent of the cloak position. Further, the dispersion properties of the cloak are explicitly specified by the refractive index of the object. The refractive-index profile of the cloak resembles that of the object implying that no strong cloak scatterers are needed. For backward scattering (observer in the half-space $z < 0$) the situation is different. In this case cloaking does not necessitate the use of amplifying or negative-index materials, but is possible only for incident fields that are superpositions of diffraction-free waves (Bessel beams) [144, 145]. Such wavefields are self-imaging fields which repeat periodically on propagation. In addition, backward cloaking depends on the position of the cloak and occurs only for certain values of a_1. We emphasize that our findings on slab cloaking do not contradict the known results on non-scattering scatterers [146, 147].

7. Conclusions and outlook

The results presented in this thesis show that both metallic and NIM superlenses allow electromagnetic near-field imaging of dipole-like objects with subwavelength resolution (Publications I–IV). The best image quality is achieved with a low-absorption slab lens having a good impedance match with its surroundings (Publications I–II). Near-field interactions among the objects and the imaging element influence the image quality: in the immediate vicinity of the slab the dipole–slab interaction prevents the dipole from radiating adversely influencing the imaging capabilities. With low-loss NIMs the interaction is weak and of short range, whereas for silver slabs it is stronger and reaches over the near-field zone. The dipole emission is also suppressed by dipole–dipole near-field interactions when the objects are close to the lens or each other, in particular with molecular objects of small size and high polarizability while the effect is weak for glass or metallic nanoparticles (Publications III–IV).

In near-field imaging two nearby objects are necessarily correlated as a result of common excitation and because of their near-field coupling. Due to the interference subwavelength resolution cannot be achieved if the object dipoles oscillate mostly parallel with the imaging element. On the other hand, if the emitters are excited such that their dipole moments are orthogonal to the slab surface, which can be accomplished by total internal reflection, resolutions well beyond the conventional diffraction limit are reached (Publication IV). The imaging capabilities of slightly lossy NIM superlenses are superior to those of metallic ones.

It is also shown in this thesis that any weakly scattering object can be perfectly cloaked in the forward direction by an absorbing NIM or amplifying positive-index medium in slab geometry (Publication V). Cloaking takes place for incident fields of arbitrary spatial structure and spectral width. In backscattering, cloaking is achievable at least for incident self-

imaging fields. In both forward and backward cloaking, the refractive-index profile of the cloak slab resembles that of the object implying that no strong scatterers are needed for cloaking.

The topics investigated in this thesis belong to fascinating, highly topical, but also very demanding research areas of modern optics. During the last ten years a variety of physical phenomena involved in superlens imaging and cloaking have been examined in theoretical studies, many of which have also been demonstrated experimentally. However, the next milestone of bringing the proposed ideas and concepts into practise, especially in the optical regime, requires further progress on metamaterials and nano-scale fabrication techniques. The results in Publications I–II are in line with earlier theoretical works and experimental demonstrations of near-field superlenses. These papers contain the most detailed formalism thus far for determining the image-intensity distribution of a single radiating point dipole, which is not a two-dimensional grating or structure used in experiments. The interactions are an inherent feature of nanoscale imaging techniques, but in the context of superlenses they have not been studied much. Therefore, the investigation on interactions reported in Publications III–IV provides useful information for the development of superlens systems, and are also valuable from the physical point of view. The research on weak scatterers in Publication V introduces the principle of cloaking from a new perspective, and thus broadens the scale of cloaking applications.

Altogether, in this thesis only a limited number of aspects concerning the research topics could be addressed. In theoretical physics approximations are made and the results are to be regarded within the realm of those approximations. Each part of the investigations in this work raises a number of important questions, many of which remain unanswered. For instance, could the proposed concepts on slab cloaking be extended to strongly scattering stratified objects, at least for beam illumination? On a more fundamental scale, what is the role of spatial dispersion in the various metamaterial structures and how does it affect near-field imaging with NIM slabs? Another task would be to include multipole terms into the scattering model of nanoparticles. Consideration of the polarization state in the image fields would provide additional information on the objects under study. In the end, the fidelity of any near-field imaging system is determined by the images of real objects it produces.

Appendix A: Basic tools of electromagnetic optics

A.1 Maxwell's equations

The behavior of an electromagnetic field in any medium is governed by the Maxwell equations. The macroscopic Maxwell equations in SI units read as [148]

$$\nabla \cdot \mathbf{D}(\mathbf{r},t) = \rho(\mathbf{r},t), \tag{A.1}$$

$$\nabla \cdot \mathbf{B}(\mathbf{r},t) = 0, \tag{A.2}$$

$$\nabla \times \mathbf{E}(\mathbf{r},t) = -\frac{\partial \mathbf{B}(\mathbf{r},t)}{\partial t}, \tag{A.3}$$

$$\nabla \times \mathbf{H}(\mathbf{r},t) = \frac{\partial \mathbf{D}(\mathbf{r},t)}{\partial t} + \mathbf{j}(\mathbf{r},t), \tag{A.4}$$

where $\mathbf{D}$ denotes the electric displacement, $\mathbf{B}$ the magnetic induction, $\mathbf{E}$ the electric field, and $\mathbf{H}$ the magnetic field. The sources of the field are the free charge density ρ and the free current density $\mathbf{j}$. They are considered as continuous functions in macroscopic electrodynamics.

The above equations are written in the space–time domain, but the electromagnetic field, and in particular its interaction with matter, are more easily analyzed in the space–frequency domain. To do this, one can use the spectral representation of time dependent fields: the spectrum $\tilde{\mathbf{F}}(\mathbf{r},\omega)$ of an arbitrary time-dependent field $\mathbf{F}(\mathbf{r},t)$ is defined by the Fourier transform. On the other hand, if $\tilde{\mathbf{F}}(\mathbf{r},\omega)$ is known, the time-dependent field can be calculated by the inverse Fourier transform [10]

$$\mathbf{F}(\mathbf{r},t) = \int_{-\infty}^{\infty} \tilde{\mathbf{F}}(\mathbf{r},\omega) e^{-\mathrm{i}\omega t} \mathrm{d}\omega. \tag{A.5}$$

Applying the Fourier transform to Eqs. (A.1)–(A.4) one obtains Maxwell's

equations in the space–frequency domain

$$\nabla \cdot \tilde{\mathbf{D}}(\mathbf{r},\omega) = \tilde{\rho}(\mathbf{r},\omega), \tag{A.6}$$

$$\nabla \cdot \tilde{\mathbf{B}}(\mathbf{r},\omega) = 0, \tag{A.7}$$

$$\nabla \times \tilde{\mathbf{E}}(\mathbf{r},\omega) = \mathrm{i}\omega\tilde{\mathbf{B}}(\mathbf{r},\omega), \tag{A.8}$$

$$\nabla \times \tilde{\mathbf{H}}(\mathbf{r},\omega) = -\mathrm{i}\omega\tilde{\mathbf{D}}(\mathbf{r},\omega) + \tilde{\mathbf{j}}(\mathbf{r},\omega), \tag{A.9}$$

which hold for the spectral components of the electromagnetic field.

A.2 Response of matter to electromagnetic fields

An electromagnetic field induces a polarization $\mathbf{P}$ and a magnetization $\mathbf{M}$ in the medium. The vectors $\mathbf{D}$ and $\mathbf{B}$ take into account this response of matter, and are connected to the polarization and magnetization according to the relations [148]

$$\mathbf{D}(\mathbf{r},t) = \epsilon_0\mathbf{E}(\mathbf{r},t) + \mathbf{P}(\mathbf{r},t), \tag{A.10}$$

$$\mathbf{B}(\mathbf{r},t) = \mu_0[\mathbf{H}(\mathbf{r},t) + \mathbf{M}(\mathbf{r},t)], \tag{A.11}$$

where ϵ_0 and μ_0 are the electric permittivity and magnetic permeability of vacuum, respectively. In general, the relation between $\mathbf{E}$ and $\mathbf{D}$ ($\mathbf{H}$ and $\mathbf{B}$) can be rather complicated. In this work, I consider the electromagnetic field in linear, isotropic, stationary, spatially non-dispersive, but temporally dispersive medium. In that case the polarization and the magnetization are connected to the electric and magnetic field via the following convolution relations [10, 149]

$$\mathbf{P}(\mathbf{r},t) = \epsilon_0 \int_{-\infty}^{t} \chi_\mathrm{e}(\mathbf{r},t-t')\mathbf{E}(\mathbf{r},t')\mathrm{d}t', \tag{A.12}$$

$$\mathbf{M}(\mathbf{r},t) = \int_{-\infty}^{t} \chi_\mathrm{m}(\mathbf{r},t-t')\mathbf{H}(\mathbf{r},t')\mathrm{d}t', \tag{A.13}$$

where the response functions χ_e and χ_m, known as the electric and magnetic susceptibilities, vanish for $t' > t$. The above equations contain a signature of causality: the polarization and the magnetization at a time t depend on the electric and magnetic fields at all time instants t' before t (origin of temporal dispersion). The medium may also be spatially dispersive (non-local medium) in which case the above relations would be convolutions over the space, as well. The effects of spatial dispersion can be observed at interfaces between two media or in metallic objects having size comparable to the mean free path of electrons [10]. However, in many cases in nanooptics the non-local effects are very weak and can be safely

ignored [10]. Applying the Fourier transform to Eqs. (A.10)–(A.13) one can write the constitutive relations in the space–frequency domain as

$$\tilde{\mathbf{D}}(\mathbf{r},\omega) = \epsilon_0 \epsilon_\mathrm{r}(\mathbf{r},\omega)\tilde{\mathbf{E}}(\mathbf{r},\omega), \tag{A.14}$$

$$\tilde{\mathbf{B}}(\mathbf{r},\omega) = \mu_0 \mu_\mathrm{r}(\mathbf{r},\omega)\tilde{\mathbf{H}}(\mathbf{r},\omega), \tag{A.15}$$

with $\epsilon_\mathrm{r} = 1 + \chi_\mathrm{e}$ and $\mu_\mathrm{r} = 1 + \chi_\mathrm{m}$ being the relative dielectric permittivity and magnetic permeability of the medium, respectively.

Besides polarization and magnetization the electromagnetic field may induce currents. The free current density in the material can be divided into two parts: the conduction current density, $\mathbf{j}_\mathrm{c}$, induced by an external field, and the source current density $\mathbf{j}_\mathrm{s}$. The conduction current density is connected to the electric component of the external field through the relation [10, 149]

$$\tilde{\mathbf{j}}_\mathrm{c}(\mathbf{r},\omega) = \sigma(\mathbf{r},\omega)\tilde{\mathbf{E}}(\mathbf{r},\omega), \tag{A.16}$$

where σ is the conductivity of the medium.

A.3 Wave equations

Starting from the Maxwell curl equations (A.3)–(A.4) and using the relations (A.10)–(A.11) for $\mathbf{D}$ and $\mathbf{B}$, one can derive the inhomogeneous wave equations in the space–time domain for both the electric and magnetic fields [10]. Correspondingly, using Maxwell's curl equations (A.8)–(A.9) with the constitutive relations (A.14)–(A.16) gives the wave equations in the space–frequency domain [10]

$$\nabla \times \nabla \times \tilde{\mathbf{E}}(\mathbf{r},\omega) - k^2(\mathbf{r},\omega)\tilde{\mathbf{E}}(\mathbf{r},\omega) = \mathrm{i}\omega\mu_0\mu_\mathrm{r}(\mathbf{r},\omega)\tilde{\mathbf{j}}_\mathrm{s}(\mathbf{r},\omega), \tag{A.17}$$

$$\nabla \times \nabla \times \tilde{\mathbf{H}}(\mathbf{r},\omega) - k^2(\mathbf{r},\omega)\tilde{\mathbf{H}}(\mathbf{r},\omega) = \nabla \times \tilde{\mathbf{j}}_\mathrm{s}(\mathbf{r},\omega), \tag{A.18}$$

where $k = k_0 n$ is the wave number in medium. Here $k_0 = \omega/c_0$ is the vacuum wave number with $c_0 = (\epsilon_0\mu_0)^{-1/2}$ being the vacuum speed of light, and $n^2 = \epsilon_\mathrm{r}\mu_\mathrm{r}$ denotes the square of the refractive index of the material, with the substitution $\epsilon_\mathrm{r} + \mathrm{i}\sigma/\omega\epsilon_0 \to \epsilon_\mathrm{r}$. These wave equations which describe the propagation of an electromagnetic field are valid also in an inhomogeneous medium.

A.4 The Green function

The Green function gives the electromagnetic field produced by a point source in a certain geometry. In a homogeneous (infinite) medium the

Green function $\overleftrightarrow{\mathbf{G}}$ satisfies the equation [10, 25]

$$\nabla \times \nabla \times \overleftrightarrow{\mathbf{G}}(\mathbf{r}, \mathbf{r}', \omega) - k^2(\omega)\overleftrightarrow{\mathbf{G}}(\mathbf{r}, \mathbf{r}', \omega) = \overleftrightarrow{\mathbf{I}}\delta(\mathbf{r} - \mathbf{r}'), \tag{A.19}$$

where $\overleftrightarrow{\mathbf{I}}$ is the unit tensor and δ denotes the delta function describing the point current source at $\mathbf{r}'$. A solution of Eq. (A.19) takes the form [10, 25]

$$\overleftrightarrow{\mathbf{G}}(\mathbf{r}, \mathbf{r}', \omega) = \left[\overleftrightarrow{\mathbf{I}} + \frac{1}{k^2}\nabla\nabla\right] G(\mathbf{r}, \mathbf{r}', \omega), \tag{A.20}$$

where

$$G(\mathbf{r}, \mathbf{r}', \omega) = \frac{e^{\mathrm{i}k|\mathbf{r}-\mathbf{r}'|}}{4\pi|\mathbf{r} - \mathbf{r}'|} \tag{A.21}$$

is the outgoing scalar Green function that satisfies the Helmholtz equation [10, 25]. In terms of the Green function the solution of Eq. (A.17) for a current distribution $\mathbf{j}_\mathrm{s}$, located in a volume V, becomes [10, 25]

$$\mathbf{E}(\mathbf{r}, \omega) = \mathbf{E}_0(\mathbf{r}, \omega) + \mathrm{i}\omega\mu_0\mu_\mathrm{r}(\omega) \int_V \overleftrightarrow{\mathbf{G}}(\mathbf{r}, \mathbf{r}', \omega)\, \mathbf{j}_\mathrm{s}(\mathbf{r}')\mathrm{d}^3r', \tag{A.22}$$

where $\mathbf{r}$ is a point located outside V. The field $\mathbf{E}_0$ represents a wave created by sources located at infinity.

In nanooptics one is often interested in the electric field generated by an electric point dipole. For the dipole located at $\mathbf{r}'$ and having the dipole moment $\mathbf{q}$ the current density has the form [10]

$$\mathbf{j}_\mathrm{s}(\mathbf{r}) = -\mathrm{i}\omega\mathbf{q}\delta(\mathbf{r} - \mathbf{r}'), \tag{A.23}$$

and the electric field can be calculated by inserting this expression into Eq. (A.22). If $\mathbf{E}_0 = 0$ one ends up with Eq. (2.1).

A.5 Monochromatic fields

A monochromatic (time-harmonic) field oscillates at a single, constant frequency. In reality no wave is strictly monochromatic, but comprises a band of frequencies. However, any field with an arbitrary time-dependence can be expressed as a superposition of monochromatic waves. Further, the temporal dispersion in an optical system can be taken into account by considering the wave propagation for monochromatic fields at different frequencies separately. Monochromatic field components at frequency ω have the form [10]

$$\mathbf{F}(\mathbf{r}, t) = \mathbf{F}(\mathbf{r}, \omega)e^{-\mathrm{i}\omega\mathrm{t}}, \tag{A.24}$$

where the spatial part $\mathbf{F}(\mathbf{r},\omega)$ is complex. For the time-harmonic fields the time-dependent Maxwell equations (A.1)–(A.4) take the form [10]

$$\nabla \cdot \mathbf{D}(\mathbf{r},\omega) = \rho(\mathbf{r},\omega), \tag{A.25}$$

$$\nabla \cdot \mathbf{B}(\mathbf{r},\omega) = 0, \tag{A.26}$$

$$\nabla \times \mathbf{E}(\mathbf{r},\omega) = \mathrm{i}\omega\mathbf{B}(\mathbf{r},\omega), \tag{A.27}$$

$$\nabla \times \mathbf{H}(\mathbf{r},\omega) = -\mathrm{i}\omega\mathbf{D}(\mathbf{r},\omega) + \mathbf{j}(\mathbf{r},\omega). \tag{A.28}$$

One can notice that these Maxwell equations are equivalent to those of the spectral components of an arbitrary time-dependent field (A.6)–(A.9). Hence, the solutions for $\mathbf{E}(\mathbf{r},\omega)$ and $\mathbf{H}(\mathbf{r},\omega)$ are identical to the solutions for $\tilde{\mathbf{E}}(\mathbf{r},\omega)$ and $\tilde{\mathbf{H}}(\mathbf{r},\omega)$.

For dielectric materials the free charge density ρ and the source current density $\mathbf{j}_\mathrm{s}$ are zero. This is valid also for materials having appreciable conductivity, i.e., for metals [45]. If further the medium is homogenous, i.e., the material parameters do not depend on $\mathbf{r}$, the wave equations (A.17)–(A.18) reduce to the homogenous Helmholtz equations [10]

$$[\nabla^2 + k^2(\omega)]\mathbf{E}(\mathbf{r},\omega) = 0, \tag{A.29}$$

$$[\nabla^2 + k^2(\omega)]\mathbf{H}(\mathbf{r},\omega) = 0. \tag{A.30}$$

The most common solution for the Helmholtz equations is the monochromatic plane wave for which the spatial part of the field has the form

$$\mathbf{E}(\mathbf{r},\omega) = \mathbf{E}_0(\omega)e^{\mathrm{i}\mathbf{k}\cdot\mathbf{r}}, \tag{A.31}$$

$$\mathbf{H}(\mathbf{r},\omega) = \mathbf{H}_0(\omega)e^{\mathrm{i}\mathbf{k}\cdot\mathbf{r}}, \tag{A.32}$$

where $\mathbf{E}_0(\omega)$ and $\mathbf{H}_0(\omega)$ are the complex electric and magnetic field amplitudes. The vector $\mathbf{k}$ is the wave vector having the property

$$\mathbf{k}\cdot\mathbf{k} = k_0^2\epsilon_\mathrm{r}(\omega)\mu_\mathrm{r}(\omega), \tag{A.33}$$

which is known as the dispersion relation.

A.6 Angular spectrum representation

The angular spectrum representation is a useful mathematical technique for studying the propagation of optical fields in homogenous media [10,38, 143, 150]. One understands the angular spectrum representation as an expansion of an optical field, in a source-free slab or half-space, in terms of plane waves with variable amplitudes and propagation directions.

Consider a monochromatic field in a slab filling the region $0 \leq z \leq Z$. All the sources are located outside the slab, and hence, the spatial part of the field satisfies the Helmholtz equations (A.29)–(A.30). I assume that in any plane with constant z inside the slab the field can be expressed as a Fourier integral

$$\mathbf{E}(x,y,z,\omega) = \iint_{-\infty}^{\infty} \mathbf{E}(k_x,k_y;z,\omega) e^{\mathrm{i}(k_x x + k_y y)} \mathrm{d}k_x \mathrm{d}k_y, \tag{A.34}$$

where k_x and k_y are spatial frequencies corresponding to the Cartesian transverse coordinates x and y, respectively. Inserting this expression into the Helmholtz equation gives the differential equation for $\mathbf{E}(k_x,k_y;z,\omega)$ [10,38]

$$\frac{\partial^2 \mathbf{E}(k_x,k_y;z,\omega)}{\partial^2 z} + k_z^2 \mathbf{E}(k_x,k_y;z,\omega) = 0, \tag{A.35}$$

where

$$k_z = +[k^2 - (k_x^2 + k_y^2)]^{1/2}, \qquad k_x^2 + k_y^2 \leq k^2, \tag{A.36}$$

$$k_z = +\mathrm{i}[(k_x^2 + k_y^2) - k^2]^{1/2}, \qquad k_x^2 + k_y^2 > k^2, \tag{A.37}$$

and $k = k_0 n$ is the wave number within the slab. Using the general solution for the differential equation (A.35) the field in the slab can be expressed as [10,38]

$$\begin{aligned}\mathbf{E}(x,y,z,\omega) = &\iint_{-\infty}^{\infty} \mathbf{A}(k_x,k_y;\omega) e^{\mathrm{i}(k_x x + k_y y + k_z z)} \mathrm{d}k_x \mathrm{d}k_y \\ &+ \iint_{-\infty}^{\infty} \mathbf{B}(k_x,k_y;\omega) e^{\mathrm{i}(k_x x + k_y y - k_z z)} \mathrm{d}k_x \mathrm{d}k_y,\end{aligned} \tag{A.38}$$

where $\mathbf{A}(k_x,k_y;\omega)$ and $\mathbf{B}(k_x,k_y;\omega)$ are arbitrary functions. This expression is known as the angular spectrum representation.

When the refractive index is real and positive, the z component of the wave vector, k_z, is either real or purely imaginary. Therefore, the formula in Eq. (A.38) represents the wave field in terms of four types of plane-wave solutions:

(i) $e^{\mathrm{i}(k_x x + k_y y)} e^{\mathrm{i}k_z z}$, with $k_z = +[k^2 - (k_x^2 + k_y^2)]^{1/2}$ and $k_x^2 + k_y^2 \leq k^2$.
These solutions are homogenous plane waves that propagate from the boundary plane $z = 0$ towards the boundary plane $z = Z > 0$.

(ii) $e^{\mathrm{i}(k_x x + k_y y)} e^{\mathrm{i}k_z z}$, with $k_z = +\mathrm{i}[k_x^2 + k_y^2 - k^2]^{1/2}$ and $k_x^2 + k_y^2 > k^2$.
These waves are inhomogenous with the amplitudes decaying exponentially from the plane $z = 0$ towards the plane $z = Z > 0$. Inhomogeneous waves of this kind are also known as evanescent waves.

(iii) $e^{\mathrm{i}(k_x x+k_y y)}e^{-\mathrm{i}k_z z}$, with $k_z = +[k^2-(k_x^2+k_y^2)]^{1/2}$ and $k_x^2+k_y^2 \leq k^2$.
These are homogenous plane waves that propagate from the boundary plane $z = Z > 0$ towards the boundary plane $z = 0$.

(iv) $e^{\mathrm{i}(k_x x+k_y y)}e^{-\mathrm{i}k_z z}$, with $k_z = +\mathrm{i}[k_x^2+k_y^2-k^2]$ and $k_x^2+k_y^2 > k^2$.
These are evanescent waves and their amplitudes decay exponentially from the plane $z = Z$ towards the plane $z = 0$.

One should note that in an absorbing material the permittivity and the permeability are complex quantities. Consequently, the wave vector becomes complex as well, and the waves decay due to absorbtion of the medium. Thus, I can no longer use the terms propagating and evanescent, but I preferably speak of slowly decaying and fast decaying waves when I refer to the waves related to low spatial frequencies (propagating) and high spatial frequencies (evanescent), respectively.

The angular spectrum representation for a field that propagates into the half-space $z \geq 0$ and whose sources are located in $z < 0$ is obtained from Eq. (A.38) by neglecting the latter term [38]. The spectral amplitudes $\mathbf{A}(k_x, k_y; \omega)$ of each plane-wave component can be expressed by the Fourier transform of the field in the plane $z = 0$. Thus, if the field is known in the plane $z = 0$, it is known throughout the half space $z > 0$ in terms of the angular spectrum representation.

A.7 Boundary conditions

The boundary conditions for the electromagnetic field at the interface between two media are conventionally derived from the integral forms of the Maxwell equations. The boundary conditions are valid for both the time-dependent fields and their spectral components, and they are of the form [10]

$$\hat{\mathbf{n}} \times (\mathbf{E}_2 - \mathbf{E}_1) = \mathbf{0}, \tag{A.39}$$

$$\hat{\mathbf{n}} \times (\mathbf{H}_2 - \mathbf{H}_1) = \mathbf{j}_{\mathrm{su}}, \tag{A.40}$$

$$\hat{\mathbf{n}} \cdot (\mathbf{D}_2 - \mathbf{D}_1) = \rho_{\mathrm{su}}, \tag{A.41}$$

$$\hat{\mathbf{n}} \cdot (\mathbf{B}_2 - \mathbf{B}_1) = 0, \tag{A.42}$$

where $\hat{\mathbf{n}}$ is the unit normal vector of the interface pointing from medium of incidence (medium 1) into medium of transmittance (medium 2). The vector $\mathbf{j}_{\mathrm{su}}$ denotes the surface current density, and ρ_{su} is the surface charge

density. The fields on both sides of the interface are connected by Maxwell's equations, and hence, the boundary conditions are not independent of each other. The surface current density, $\mathbf{j}_{\mathrm{su}}$, and the surface charge density, ρ_{su}, vanish in the case of any real materials because they are not perfectly conducting [45].

A.8 Fresnel's coefficients

When light propagates across an interface between two media, reflection and refraction take place. The Fresnel reflection and transmission coefficients, $r_{\mathrm{s,p}}$ and $t_{\mathrm{s,p}}$, respectively, describe how the amplitude and phase of a plane wave are changed in reflection and transmission. These coefficients are usually derived for s and p polarizations from the boundary conditions and they read as [10, 45, 148]

$$r_{\mathrm{s}}(k_x, k_y, \omega) = \frac{\mu_{\mathrm{r},2}(\omega)k_{z,1}(\omega) - \mu_{\mathrm{r},1}(\omega)k_{z,2}(\omega)}{\mu_{\mathrm{r},2}(\omega)k_{z,1}(\omega) + \mu_{\mathrm{r},1}(\omega)k_{z,2}(\omega)}, \tag{A.43}$$

$$t_{\mathrm{s}}(k_x, k_y, \omega) = \frac{2\mu_{\mathrm{r},2}(\omega)k_{z,1}(\omega)}{\mu_{\mathrm{r},2}(\omega)k_{z,1}(\omega) + \mu_{\mathrm{r},1}(\omega)k_{z,2}(\omega)}, \tag{A.44}$$

$$r_{\mathrm{p}}(k_x, k_y, \omega) = \frac{\epsilon_{\mathrm{r},2}(\omega)k_{z,1}(\omega) - \epsilon_{\mathrm{r},1}(\omega)k_{z,2}(\omega)}{\epsilon_{\mathrm{r},2}(\omega)k_{z,1}(\omega) + \epsilon_{\mathrm{r},1}(\omega)k_{z,2}(\omega)}, \tag{A.45}$$

$$t_{\mathrm{p}}(k_x, k_y, \omega) = \frac{2\epsilon_{\mathrm{r},2}(\omega)k_{z,1}(\omega)}{\epsilon_{\mathrm{r},2}(\omega)k_{z,1}(\omega) + \epsilon_{\mathrm{r},1}(\omega)k_{z,2}(\omega)}\sqrt{\frac{\mu_{\mathrm{r},2}(\omega)\epsilon_{\mathrm{r},1}(\omega)}{\mu_{\mathrm{r},1}(\omega)\epsilon_{\mathrm{r},2}(\omega)}}, \tag{A.46}$$

where the subscript 1 denotes the medium of incidence and the subscript 2 refers to the medium of transmittance. The Fresnel coefficients are valid for both the propagating and evanescent waves.

I note that unlike commonly perceived, the Fresnel transmission coefficient t_p in Eq. (A.46) is not, in general, the ratio of the complex amplitude of the transmitted field to that of the incident field. If the unit vector $\hat{\mathbf{p}}$ specifying the p-polarized electric field component is complex, which happens for evanescent fields and when one or both of the media are lossy, $\hat{\mathbf{p}}$ is not normalized in the sense of complex-valued vectors [41, 62].

References

[1] V. G. Veselago, "The electrodynamics of substances with simultaneously negative values of ϵ and μ", Sov. Phys. Usp. **10**, 509–514 (1968).

[2] R. Marques, F. Martin, and M. Sorolla, *Metamaterials with Negative Parameters: Theory, Design, and Microwave Applications* (Wiley, Hoboken, 2008).

[3] L. Solymar and E. Shamonina, *Waves in Metamaterials* (Oxford University Press, New York, 2009).

[4] V. M. Shalaev, "Optical negative-index metamaterials", Nature Photon. **1**, 41–48 (2007).

[5] C. M. Soukoulis, S. Linden, and M. Wegener, "Negative refractive index at optical wavelengths", Science **315**, 47–49 (2007).

[6] Y. Liu and X. Zhang, "Metamaterials: a new frontier of science and technology", Chem. Soc. Rev. **40**, 2494–2507 (2011).

[7] X. Zhang and Z. Liu, "Superlenses to overcome the diffraction limi", Nature Mater. **7**, 435–441 (2008).

[8] V. M. Shalaev, "Transforming light", Science **322**, 384–386 (2008).

[9] H. Chen, C. T. Chan, and P. Sheng, "Transformation optics and metamaterials", Nature Mater. **9**, 387–396 (2010).

[10] L. Novotny and B. Hecht, *Principles of Nano-Optics* (Cambridge University Press, Cambridge, 2006).

[11] L. Novotny, "The history of near-field optics", in *Progress in Optics*, ed. E. Wolf (Elsevier, Amsterdam, 2007), vol. 50, pp. 137–184.

[12] D. Courjon, *Near-Field Microscopy and Near-Field Optics* (Imperial College Press, London, 2003).

[13] J. B. Pendry, "Negative refraction makes a perfect lens", Phys. Rev. Lett. **85**, 3966–3969 (2000).

[14] N. Fang, H. Lee, C. Sun, and X. Zhang, "Sub-diffraction-limited imaging with a silver superlenses", Science **308**, 534–537 (2005).

[15] H. Lee, Y. Xiong, N. Fang, W. Srituravanich, S. Durant, M. Ambati, C. Sun, and X. Zhang, "Realization of optical superlens imaging below the diffraction limit", New J. Phys. **7**, 255 (2005).

[16] P. Chaturvedi, W. Wu, V. J. Logeeswaran, Z. Yu, M. S. Islam, S. Y. Wang, R. S. Williams, and N. X. Fang, "A smooth optical superlens", Appl. Phys. Lett. **96**, 043102 (2010).

[17] U. Leonhardt, "Optical conformal mapping", Science **312**, 1777–1780 (2006).

[18] J. B. Pendry, D. Schurig, and D. R. Smith, "Controlling electromagnetic fields", Science **312**, 1780–1782 (2006).

[19] D. Schurig, J. J. Mock, B. J. Justice, S. A. Cummer, J. B. Pendry, A. F. Starr, and D. R. Smith, "Metamaterial electromagnetic cloak at microwave frequencies", Science **314**, 977–980 (2006).

[20] J. Valentine, J. Li, T. Zentgraf, G. Bartal, and X. Zhang, "An optical cloak made of dielectrics", Nature Mater. **8**, 568–571 (2009).

[21] L. H. Gabricelli, J. Cardenas, C. B. Poitras, and M. Lipson, "Silicon nanostructure cloak operating at optical frequencies", Nature Photon. **3**, 461–463 (2009).

[22] T. Ergin, N. Stenger, P. Brenner, J. B. Pendry, and M. Wegener, "Three-dimensional invisibility cloak at optical wavelengths", Science **328**, 337–339 (2010).

[23] M. W McGall, A Farfaro, P. Kinrles, and A. Boardman, "A spacetime cloak or a history editor", J. Opt. **13**, 024003 (2011).

[24] M. Fridman, A. Farsi, Y. Okawachi, and A. L. Gaeta, "Demonstration of temporal cloaking", Nature Lett. **481**, 62–65 (2012).

[25] C.-T. Tai, *Dyadic Green's Functions in Electromagnetic Theory* (Intext, Scranton, 1971).

[26] G. F. Bohren and D. R. Huffman, *Absorption and Scattering of Light by Small Particles* (Wiley, New York, 1998).

[27] R. Carminati, J.-J. Greffet, C. Henkel, and J. M. Vigoureux, "Radiative and non-radiative decay of a single molecule close to a metallic nanoparticle", Opt. Commun. **261**, 368–375 (2006).

[28] M. Fox, *Quantum Optics: An Introduction* (Oxford University Press, Oxford, 2006).

[29] J. Grondalski and D. F. V. James, "Is there a fundamental limitation on the measurements of spatial coherence for highly incoherent fields", Opt. Lett. **28**, 1630–1632 (2003).

[30] O. Keller, M. Xiao, and S. Bozhevolnyi, "Configurational resonances in optical near-field microscopy: a rigorous point-dipole approach", Surf. Sci. **280**, 217–230 (1993).

[31] E. M. Purcell and C. R. Pennypacker, "Scattering and absorbtion of light by nonspherical dielectric grains", Astrophys. J. **186**, 705–714 (1973).

[32] B. T. Draine, "The discrete dipole approximation and its application to interstellar graphite grains", Astrophys. J. **333**, 848–872 (1988).

[33] B. T. Draine and J. Goodman, "Beyond Clausius-Mossotti: Wave propagation on a polarizable point lattice and the discrete dipole approximation", Astrophys. J. **405**, 685–697 (1993).

[34] B. T. Draine and P. J. Flatau, "Discrete-dipole approximation for scattering calculations", J. Opt. Soc. Am. A **11**, 1491–1499 (1994).

[35] M. A. Yurkin and A. G. Hoekstra, "The discrete dipole approximation: an overview and recent developments", J. Quant. Spectrosc. Radiat. Transfer **106**, 558–589 (2007).

[36] M. A. Yurkin and A. G. Hoekstra, "The discrete dipole approximation code ADDA: Capabilities and known limitations", J. Quant. Spectrosc. Radiat. Transfer **112**, 2234–2247 (2011).

[37] G. J. Gbur, *Mathematical Methods for Optical Physics and Engineering* (Cambridge University Press, New York, 2011).

[38] L. Mandel and E. Wolf, *Optical Coherence and Quantum Optics* (Cambridge University Press, Cambridge, 1995).

[39] K.-H. Brenner, "Plane wave decomposition in layered materials and meta-materials", in *6th International Workshop on Information Optics (WIO '07)*, eds. J. A. Benediktsson, B. Javidi, and K. S. Gudmunsson, AIP Conference Proc. **949**, 59–66 (2007).

[40] J. E. Sipe, "New Green-function formalism for surface optics", J. Opt. Soc. Am. B **4**, 481–489 (1987).

[41] A. Norrman, T. Setälä, and A. T. Friberg, "Partial spatial coherence and partial polarization in random evanescent fields on lossless interfaces", J. Opt. Soc. Am. A **28**, 391–400 (2011).

[42] G. W. 't Hooft, "Comment on 'Negative refraction makes a perfect lens' ", Phys. Rev. Lett. **87**, 249701 (2001).

[43] J. B. Pendry, "Reply to the comment by G. W. 't Hooft", Phys. Rev. Lett. **87**, 249702 (2001).

[44] P. M. Morse and H. Feshbach, *Methods of Theoretical Physics* (McGraw-Hill, New York, 1953).

[45] M. Born and E. Wolf, *Principles of Optics*, 7th ed. (Cambridge University Press, Cambridge, 1999).

[46] P. B. Johnson and R. W. Christy, "Optical constants of the noble metals", Phys. Rev. B **6**, 4370–4379 (1972).

[47] A. Moroz, "Non-radiative decay of a dipole emitter close to a metallic nanoparticle: Importance of higher-order multipole contributions", Opt. Commun. **283**, 2277–2287 (2010).

[48] S. Kawata, *Near-Field Optics and Surface Plasmon Polaritons* (Springer, Heidelberg, 2001).

[49] H. Raether, *Surface Plasmons on Smooth and Rough Surfaces and on Gratings* (Springer, Berlin, 1988).

[50] S. A. Maier and H. A. Atwater, "Plasmonics: Localization and guiding of electromagnetic energy in metal/dielectric structures", J. Appl. Phys. **98**, 011101 (2005).

[51] J. M. Pitarke, V. M. Silkin, E. V. Chulnov, and P. M. Echenique, "Theory of surface plasmons and surface plasmon polaritons", Rep. Prog. Phys. **70**, 1–87 (2007).

[52] D. Sarid and W. Challener, *Modern Introduction to Surface Plasmons* (Cambridge University Press, Cambridge, 2010).

[53] A. V. Zayats, I. I. Smolyaninov, and A. A. Maradudin, "Nano-optics of surface plasmon polaritons", Phys. Rep. **408**, 131–314 (2005).

[54] P. Berini, "Long-range surface plasmon polaritons", Adv. Opt. Phot. **1**, 484–588 (2009).

[55] C. Genet and T. W. Ebbesen, "Light in tiny holes", Nature **445**, 39–46 (2007).

[56] S. Lal, S. Link, and N. J. Halas, "Nano-optics from sensing to waveguiding", Nature Phot. **1**, 641–648 (2007).

[57] J. Heber, "Surfing the wave", Nature **461**, 720–722 (2009).

[58] M. Ozaki, J.-I. Kato, and S. Kawata, "Surface-plasmon holography with white-light illumination", Science **332**, 218–220 (2011).

[59] D. K. Gramotnev and S. I. Bozhevolnyi, "Plasmonics beyond the diffraction limit", Nature Photon. **4**, 83–91 (2010).

[60] M. I. Stockman, "Nanophotonics: past, present, and glimpse into future", Opt. Express **19**, 22029–22106 (2011).

[61] S. A. Ramakrishna, "Physics of negative refractive index materials", Rep. Prog. Phys. **68**, 449–521 (2005).

[62] L. D. Landau and E. M. Lifshitz, *Electrodynamics of Continuous Media*, 2nd ed. (Pergamon Press, Oxford, 1981).

[63] J. B. Pendry, A. J. Holden, D. J. Robbins, and W. J. Stewart, "Magnetism from conductors and enhanced nonlinear phenomena", IEEE Trans. Microwave Theory Tech. **47**, 2075–2084 (1999).

[64] D. R. Smith, W. J. Padilla, D. C. Vier, S. C. Nemat-Nasser, and S. Schultz, "Composite medium with simultaneously negative permeability and permittivity", Phys. Rev. Lett. **84**, 4184–4187 (2000).

[65] L. V. Panina, A. N. Grigorenko, and D. P. Makhnovskiy, "Optomagnetic composite medium with conducting nanoelement", Phys. Rev. B **66**, 155411 (2002).

[66] A. Ishikawa, T. Tanaka, and S. Kawata, "Negative magnetic permeability in the visible light region", Phys. Rev. Lett. **95**, 237401 (2005).

[67] M. Kafesaki, I. Tsiapa, N. Katsarakis, Th. Koschny, C. M. Soukoulis, and E. N. Economou, “Left-handed metamaterials: The fishnet structure and its variations”, Phys. Rev. B **75**, 235114 (2007).

[68] D. R. Smith, S. Schultz, P. Markos, and C. M. Soukoulis, “Determination of effective permittivity and permeability of metamaterials from reflection and transmission coefficients”, Phys. Rev. B **65**, 195104 (2002).

[69] D. R. Smith, D. C. Vier, Th. Koschny, and C. M. Soukoulis, “Electromagnetic parameter retrieval from inhomogeneous metamaterials”, Phys. Rev. E **71**, 036617 (2005).

[70] C. Menzel, T. Paul, C. Rockstuhl, T. Pertsch, S. Tretyakov, and F. Lederer, “Validity of effective material parameters for optical fishnet metamaterials”, Phys. Rev. B **81**, 035320 (2010).

[71] R. A. Shelby, D. R. Smith, and S. Schultz, “Experimental verification of a negative index of refraction”, Science **292**, 77–79 (2001).

[72] C. G. Parazzoli, R. B. Greegor, K. Li, B. E. C. Koltenbah, and M. Tanielian, “Experimental verification and simulation of negative index of refraction using Snell’s law”, Phys. Rev. Lett. **90**, 107401 (2003).

[73] T. J. Yen, W. J. Padilla, N. Fang, D. C. Vier, D. R. Smith, J. B. Pendry, D. N. Basov, and X. Zhang, "Terahertz magnetic response from artificial materials”, Science **303**, 1494–1496 (2004).

[74] S. Linden, C. Enkrich, M. Wegener, J. Zhou, T. Koschny, C. M. Soukoulis, “Magnetic response of metamaterials at 100 terahertz”, Science **306**, 1351–1353 (2004).

[75] S. Zhang, W. Fan, B. K. Minhas, A. Frauenglass, K. J. Malloy, and S. R. J. Brueck, “Midinfrared resonant magnetic nanostructures exhibiting a negative permeability”, Phys. Rev. Lett. **94**, 037402 (2005).

[76] C. Enkrich, M. Wegener, S. Linden, S. Burger, L. Zschiedrich, F. Schmidt, J. F. Zhou, T. Koschny, and C. M. Soukoulis, “Magnetic metamaterials at telecommunication and visible frequencies”, Phys. Rev. Lett. **95**, 203901 (2005).

[77] J. Zhou, Th. Koschny, M. Kafesaki, E. N. Economou, J. B. Pendry, and C. M. Soukoulis, “Saturation of the magnetic response of split-ring resonators at optical frequencies”, Phys. Rev. Lett. **95**, 223902 (2005).

[78] S. Tretyakov, “On geometrical scaling of split-ring and double-bar resonators at optical frequencies”, Metamaterials **1**, 40-43 (2007).

[79] V. M. Shalaev, W. Cai, U. K. Chettiar, H.-K. Yuan, A. K. Sarychev, V. P. Drachev, and A. V. Kildishev, “Negative index of refraction in optical metamaterials”, Opt. Lett. **30**, 3356–3358 (2005).

[80] G. Dolling, C. Enkrich, M. Wegener, J. F. Zhou, C. M. Soukoulis, and S. Linden, “Cut-wire pairs and plate pairs as magnetic atoms for optical metamaterials”, Opt. Lett. **30**, 3198–3200 (2005).

[81] A. Ishikawa, T. Tanaka, and S. Kawata, “Magentic excitation of magnetic resonance in metamaterials at far-infrared frequencies”, Appl. Phys. Lett. **91**, 113118 (2007).

[82] J. Yao, Z. Liu, Y. Liu, Y. Wang, C. Sun, G. Bartal, A. M. Stacy, and X. Zhang, “Optical negative refraction in bulk metamaterials of nanowires”, Science **321**, 930 (2008).

[83] G. Dolling, C. Enkrich, M. Wegener, C. M. Soukoulis, and S. Linden, “Simultaneous negative phase velocity of light in a metamaterial”, Science **312**, 892–894 (2006).

[84] G. Dolling, M. Wegener, C. M. Soukoulis, S. T. Linden, “Negative-index at 780 nm wavelength”, Opt. Lett. **32**, 53–55 (2007).

[85] U. K. Chettiar, A. V. Kildishev, H. K. Yuan, W. Cai, S. Xiao, V. P. Drachev, V. M. Shalaev, “Dual-band negative index metamaterial: double negative at 813 nm and single negative at 772 nm”, Opt. Lett. **32**, 1671–1673 (2007).

[86] J. Valentine, S. Zhang, T. Zentgraf, E. Ulin-Avila, D. A. Genov, G. Bartal, and X. Zhang, “Three-dimensional optical metamaterial with a negative refractive index”, Nature **455**, 376–379 (2008).

[87] S. M. Xiao, U. K. Chettiar, A. V. Kildishev, V. P. Drachev, and V. M. Shalaev, “Yellow-light negative-index metamaterials”, Opt. Lett. **34**, 3478–3480 (2009).

[88] J. Valentine, S. Zhang, T. Zentgraf, and X. Zhang, “Development of bulk optical negative index fishnet metamaterials: Achieving a low-loss and broadband response through coupling”, Proc. IEEE **99**, 1682–1690 (2011).

[89] S. A. Ramakrishna and J. B. Pendry, “Removal of absorption and increase in resolution in a near-field lens via optical gain”, Phys. Rev. B **67**, 201101(R) (2003).

[90] A. Xiao, V. P. Drachev, A. V. Kildishev, X. Ni, U. K. Chettiar, H-K. Yuan, and V. M. Shalaev, “Loss-free and active optical negative-index metamaterials”, Nature **466**, 735–738 (2010).

[91] S. Tretyakov, I. Nefedov, A. Sihvola, S. Maslovski, and C. Simovski, “Wave and energy in chiral nihility”, J. Electromagn. Waves Appl. **17**, 695–706 (2003).

[92] J. B. Pendy, “A chiral route to negative refaction”, Science **306**, 1353–1355 (2004).

[93] S. Zhang, Y.-S. Park, J. Li, X. Lu, W. Zhang, and X. Zhang, “Negative refractive index in chiral metamaterials”, Phys. Rev. Lett. **102**, 023901 (2009).

[94] M. J. Huttunen, G. Bautista, M. Decker, S. Linden, M. Wegener, and M. Kauranen, “Nonlinear chiral imaging of subwavelength-sized twisted-cross gold nanodimers”, Opt. Mat. Exp. **1**, 46–56 (2011).

[95] A. J. Hoffman, L. Alekseyev, S. S. Howard, K. J. Franz, D. Wasserman, V. A. Podolskiy, E. E. Narimanov, D. L. Sivco, and C. Gmachl, “Negative refraction in semiconductor metamaterials”, Nature Mat. **6**, 946–950 (2007).

[96] P-Y. Chen, M. Farhat, and A. Alu, “Bistable and self-tunable negative-index metamaterial at optical frequencies”, Phys. Rev. Lett. **106**, 105503 (2011).

[97] S. A. Ramakrishna and O. J. F. Martin, “Resolving the wave vector in negative refractive index media”, Opt. Lett. **30**, 2626–2628 (2005).

[98] M. C. K. Wiltshire, J. B. Pendry, I. R. Young, D. J. Larkman, D. J. Gilderdale, and J. V. Hajnal, “Microstructured magnetic materials

for RF flux guides in magnetic resonance imaging", Science **291**, 849–851 (2001).

[99] A. Alu and N. Engheta, "Guided modes in a waveguide filled with a pair of single-negative (SNG), double-negative (DNG), and/or double-positive (DPS) layers", IEEE Trans. Microwave Theory Tech. **52**, 199–210 (2004).

[100] C. Caloz, A. Sanada, and T. Itoh, "A novel composite right-/left-handed coupled-line directional coupler with arbitrary coupling level and broad bandwidth", IEEE Trans. Microwave Theory Tech. **52**, 980–992 (2004).

[101] A. Kurs, A. Karalis, R. Moffatt, J. D. Joannopoulos, P. Fisher, and M. Soljacic, "Wireless power transfer via strongly coupled magnetic resonances", Science **317**, 83–86 (2007).

[102] H.-T. Chen, J. F. O'hara, A. K. Azad, A. J. Taylor, R. D. Averitt, D. B. Shrekenhamer, and W. J. Padilla, "Experimental demonstration of frequency-agile terahertz metamaterials", Nature Photon. **2**, 295–298 (2008).

[103] N. I. Landy, S. Sajuyigbe, J. J. Mock, D. R. Smith, and W. J. Padilla, "Perfect metamaterial absorber", Phys Rev. Lett. **100**, 207402 (2008).

[104] B. Richards and E. Wolf, "Electromagnetic diffraction in optical systems — II. Structure of the focal region", Prog. Roy. Soc. A **253**, 358–379 (1959).

[105] W. T. Welford, *Aberrations of Optical Systems* (Taylor & Francis, New York, 1986).

[106] C. J. R. Sheppard and T. Wilson, "The image of a single point in microscopes of large numerical aperture", Proc. Roy. Soc. A **379**, 145–158 (1982).

[107] J. Enderlein, "Theoretical study of detection of a dipole emitter through an objective with high numerical aperture", Opt. Lett. **25**, 634–636 (2000).

[108] J. W. Goodman, *Introduction to Fourier Optics*, 3rd ed. (Roberts & Company, Englewood, 2005).

[109] J. M. Williams, “Comment on ‘Negative refraction makes a perfect lens’ Some problems with negative refraction”, Phys. Rev. Lett. **87**, 249703 (2001).

[110] J. Pendry, “Reply to the comment by J. M. Williams”, Phys. Rev. Lett. **87**, 249704 (2001).

[111] N. Garcia and M. Nieto-Vesperinas, “Left-handed materials do not make a perfect lens”, Phys. Rev. Lett. **88**, 207403 (2002).

[112] J. Pendry, “Comment on ‘Left-handed materials do not make a perfect lens’ ”, Phys. Rev. Lett. **91**, 099701 (2003).

[113] M. Nieto-Vesperinas and N. Garcia, “Reply to the comment by J. Pendry”, Phys. Rev. Lett. **91**, 099702 (2003).

[114] M. Nieto-Vesperinas, “Problem of image superresolution with a negative-index slab”, J. Opt. Soc. Am. A **21**, 491–498 (2004).

[115] J. T. Shen and P. M. Platzman, “Near field imaging with negative dielectric constant lenses”, Appl. Phys. Lett. **80**, 3286–3288 (2002).

[116] D. R. Smith, D. Shurig, M. Rosenbluth, S. Schultz, S. A. Ramakrishna, and J. Pendry, “Limitations on subdiffraction imaging with a negative refractive index slab”, Appl. Phys. Lett. **82**, 1506–1508 (2003).

[117] I. A. Larkin and M. I. Stockman, “Imperfect perfect lens”, Nano Lett. **5**, 339–343 (2005).

[118] V. A. Podolskiy and E. E. Narimanov, “Near-sighted superlens”, Opt. Lett. **30**, 75–77 (2005).

[119] V. A Podolskiy, N. A. Kuhta, and G. W. Milton, “Optimizing the superlens: manipulating geometry to enhance the resolution”, Appl. Phys. Lett. **87**, 231113 (2005).

[120] Z. Liu, N. Fang, T.-J. Yen, and X. Zhang, “Rapid growth of evanescent wave by silver superlens”, Appl. Phys. Lett. **83**, 5184–5186 (2003).

[121] A. Giannattasio, I. R. Hooper, and W. L. Barnes, “Transmission of light through thin silver films via surface plasmon-polaritons”, Opt. Express **12**, 5881–5886 (2004).

[122] A. A. Houck, J. B. Brock, and I. L. Chuang, "Experimental observations of a left-handed material that obeys Snell's law", Phys. Rev. Lett. **90**, 137401 (2003).

[123] A. Grbic and G. V. Eleftheriades, "Overcoming the diffraction limit with a planar left-handed transmission-line lens", Phys. Rev. Lett. **92**, 117403 (2004).

[124] A. N. Lagarkov and V. N. Kissel, "Near-perfect imaging in a focusing system based on a left-handed material plate", Phys. Rev. Lett. **92**, 077401 (2004).

[125] T. Taubner, D. Korobkin, Y. Urzhumov, G. Shevts, and R. Hillenbrand, "Near-field microscopy through a SiC superlens", Science **313**, 1595 (2006).

[126] S. Durant, Z. Liu, J. M. Steele, and X. Zhang, "Theory of the transmission properties of an optical far-field superlens for imaging beyond the diffraction limit", J. Opt. Soc. Am. B **23**, 2383–2392 (2006).

[127] J. B. Pendry, "Perfect cylindrical lenses", Opt. Express **11**, 755–760 (2003).

[128] Y. Xiong, Z. Liu, C. Sun, and X. Zhang, "Two-dimensional imaging by far-field superlens at visible wavelengths", Nano Lett. **7**, 3360–3365 (2007).

[129] Z. Liu, H. Lee, Y. Xiong, C. Sun, X. Zhang, "Far-field optical hyperlens magnifying sub-diffraction-limited objects", Science **315**, 1686 (2007).

[130] P. C. Chaumet, A. Rahmani, F. de Fornel, and J.-P. Dufour, "Evanescent light scattering: The validity of the dipole approximation", Phys. Rev. B **58**, 2310–2315 (1998).

[131] U. Leonhardt and T. Tyc, "Broadband invisibility by non-euclidean cloaking", Science **323**, 110–112 (2009).

[132] W. Yan, M. Yan, Z. Ruan, and M. Qiu, "Coordinate transformations make perfect invisibility cloaks with arbitrary shape", New J. Phys. **10**, 043040 (2008).

[133] A. Nicolet, F. Zolla, and S. Guenneau, "Electromagnetic analysis of cylindrical cloaks of an arbitrary cross section", Opt. Lett. **33**, 1584–1586 (2008).

[134] H. Ma, S. Qu, Z. Xu, and J. Wang, "Numerical method for designing approximate cloaks with arbitrary shapes", Phys. Rev. E **78**, 036608 (2008).

[135] J. Li and J. B. Pendry, "Hiding under the carpet: a new strategy for cloaking", Phys. Rev. Lett. **101**, 203901 (2008).

[136] H. F. Ma and T. J. Cui, "Three-dimensional broadband ground-plane cloak made of metamaterials", Nature Commun. **1**, 1–6 (2010).

[137] M. G. Silverinha, A. Alu, and N. Engheta, "Parallel-pate metamaterials for cloaking structures", Phys. Rev. E **75**, 036603 (2007).

[138] S. Tretyakov, P. Alitalo, O. Luukkonen, and C. Simovski, "Broadband electromagnetic cloaking of long cylindrical objects", Phys. Rev. Lett. **103**, 103905 (2009).

[139] F. J. Garcia de Abajo, G. Gomez-Santos, L. A. Blanco, A. G. Borisov, and S. V. Shabanov, "Tunneling mechanism of light transmission through metallic films", Phys. Rev. Lett. **95**, 067403 (2005).

[140] N.-A. P. Nicorovici, G. W. Milton, R. C. McPhedran, L. Botten, "Quasistatic cloaking of two-dimensional polarizable discrete systems by anomalous resonance", Opt. Express **15**, 6314-6323 (2007).

[141] X. Chen, Y. Luo, J. Zhang, K. Jiang, J. B. Pendry, and S. Zhang, "Macroscopic invisibility cloaking of visible light", Nature Commun. **2**, 1–6 (2011).

[142] Y. Lai, H. Chen, Z.-Q. Zhang, and C. T. Tan, "Complementary media invisibility cloak that cloaks objects at a distance outside the cloaking shell", Phys. Rev. Lett. **102**, 093901 (2009).

[143] M. Nieto-Vesperinas, *Scattering and Diffraction in Physical Optics* (Wiley, New York, 1991).

[144] A. Hakola, T. Hakkarainen, R. Tommila, and T. Kajava, "Energetic Bessel-Gauss pulses from diode-pumped solid-state lasers", J. Opt. Soc. Am. B **27**, 2342–2349 (2010).

[145] J. Turunen and A. T. Friberg, "Propagation-invariant optical fields", in *Progress in Optics*, ed. E. Wolf (Elsevier, Amsterdam, 2009), vol. 54, pp. 1–88.

[146] G. Gbur, “Nonradiating sources and other invisible objects”, in *Progress in Optics*, ed. E. Wolf (Elsevier, Amsterdam, 2003), vol. 45, pp. 273–315.

[147] B. J. Hoenders, “The uniqueness of inverse problems”, in *Inverse Source Problems in Optics*, ed. H. P. Baltes (Springer, Berlin, 1978), pp. 41–82.

[148] J. D. Jackson, *Classical Electrodynamics*, 3rd ed. (Wiley, New York, 1999).

[149] T. B. Hansen and A. D. Yaghjian, *Plane-Wave Theory of Time-Domain Fields* (IEEE Press, New York, 1999).

[150] M. Fertig and K.-H. Brenner, “Vector wave propagation method”, J Opt. Soc. Am A **27**, 709–717 (2010).

Errata

Publication I

There are misprints in Eqs. (26), (27), and (29). On the right-hand side of these equations the minus signs in front of the brackets should be located right after the equal signs.

Aalto-DD 151/2012

ISBN 978-952-60-4868-0
ISBN 978-952-60-4869-7 (pdf)
ISSN-L 1799-4934
ISSN 1799-4934
ISSN 1799-4942 (pdf)

Aalto University
School of Science
Department of Applied Physics
www.aalto.fi

BUSINESS +
ECONOMY

ART +
DESIGN +
ARCHITECTURE

SCIENCE +
TECHNOLOGY

CROSSOVER

**DOCTORAL
DISSERTATIONS**